Monthly Notices of the ROYAL ASTRONOMICAL SOCIETY

MNRAS **496,** 5052–5071 (2020) doi:10.1093/mnras/staa1871
Advance Access publication 2020 June 30

Thermal luminosities of cooling neutron stars

A. Y. Potekhin [1]★ D. A. Zyuzin [1] D. G. Yakovlev,[1] M. V. Beznogov[2] and Yu. A. Shibanov[1]

[1]*Ioffe Institute, Politekhnicheskaya 26, 194021 St Petersburg, Russia*
[2]*Instituto de Astronomia, Universidad Nacional Autonoma de Mexico, Mexico D.F. 04510, Mexico*

Accepted 2020 June 24. Received 2020 June 19; in original form 2020 May 17

ABSTRACT

Ages and thermal luminosities of neutron stars, inferred from observations, can be interpreted with the aid of the neutron star cooling theory to gain information on the properties of superdense matter in neutron-star interiors. We present a survey of estimated ages, surface temperatures, and thermal luminosities of middle-aged neutron stars with relatively weak or moderately strong magnetic fields, which can be useful for these purposes. The catalogue includes results selected from the literature, supplemented with new results of spectral analysis of a few cooling neutron stars. The data are compared with the theory. We show that overall agreement of theoretical cooling curves with observations improves substantially for models where neutron superfluidity in stellar core is weak.

Key words: radiation mechanisms: thermal – catalogues – stars: neutron – X-rays: stars.

1 INTRODUCTION

Comparison of the theory of neutron star cooling with observations can provide a wealth of important information. Since the cooling depends on neutron star properties, for example, mass, equation of state (EoS), composition of the stellar core and outer envelopes, magnetic field strength and configuration, such a comparison can help to determine some parameters of neutron stars and choose among theoretical models of superdense matter.

Using the growing number of high-quality observations of thermal radiation of neutron stars requires a catalogue of their basic observable parameters relevant to cooling – first of all, ages and thermal luminosities. Some compilations have been done in the past, embedded in reviews of the neutron star cooling theory (e.g. Yakovlev & Pethick 2004; Page 2009; Tsuruta 2009; Potekhin, Pons & Page 2015 and references therein) or in research papers (e.g. Page et al. 2004; Zhu et al. 2011; Viganò et al. 2013; Beznogov & Yakovlev 2015). Here, we revisit the collection of observational data on cooling neutron stars from the literature, including new results and reanalysing some of the archival data. We compose an updated catalogue of observational estimates of the basic properties of thermally emitting, cooling isolated neutron stars (INSs). We also present examples of such a comparison, taking some recent progress of the neutron star theory into account.

In Section 2, we sketch the basic concepts of the neutron star cooling theory. In Section 3, we present the brief summary of modern observations of thermally emitting, middle-aged INSs and list their estimated parameters that can be useful for theoretical interpretation of the data. In Section 4, we discuss some examples of the comparison of theory and observations. We summarize in Section 5.

★ E-mail: palex@astro.ioffe.ru

2 THEORETICAL BACKGROUND

The cooling theory requires constructing the models of neutron star structure and thermal evolution. This task is unique in the complexity of underlying physics (partially uncertain), ranges of temperatures and densities, and physical processes involved. Detailed reviews were given, e.g. by Yakovlev & Pethick (2004), Page (2009), Tsuruta (2009), and Potekhin et al. (2015). In this section, we outline the basic concepts of this theory.

2.1 Hydrostatic and thermal structure and evolution

Neutron stars are relativistic objects. The importance of General Relativity effects is characterized by the compactness ratio r_g/R, where R is the stellar radius, $r_g = 2GM/c^2$ is the Schwarzschild radius, M is the gravitational stellar mass, G is the Newtonian gravitational constant, and c is the speed of light. Typically, $r_g/R \sim 0.2$–0.5 for neutron stars, while $r_g/R \ll 10^{-3}$ for all other stars.

The mass density ρ ranges from small values in the atmospheres to $\rho \gtrsim 10^{15}\,\mathrm{g\,cm^{-3}}$ at the centre of a sufficiently massive neutron star (e.g. Haensel, Potekhin & Yakovlev 2007). A thin atmosphere covers the ocean, filled with a Coulomb liquid of atomic nuclei and degenerate electrons, which lies on the crust, where the nuclei are arranged in a crystalline lattice. In addition to the nuclei and electrons, there are quasi-free 'dripped' neutrons in the inner crust, at $4.3 \times 10^{11}\,\mathrm{g\,cm^{-3}}$. At ρ around $10^{14}\,\mathrm{g\,cm^{-3}}$, the clusters of nucleons may take exotic non-spherical shapes, forming a liquid-crystal mantle of the star. At still higher densities, there is a neutron-rich liquid core. The central part of sufficiently massive neutron stars (at $\rho \gtrsim 7 \times 10^{14}\,\mathrm{g\,cm^{-3}}$) has rather unknown composition and EoS, which remains a fundamental physical problem. Nucleons (and other baryons if available) in neutron star interiors can be superfluid. Neutron stars can be fast rotators (with spin periods

$\mathcal{P}$ down to $\sim$1 ms) and possess strong magnetic fields (up to $B \gtrsim 10^{15}$ G, with typical values $B \sim 10^{12}$ G).

Neutron stars cool down mainly via neutrino emission from their cores and photon emission from their atmospheres. While cooling they lose their thermal energy. They may also be reheated by various mechanisms (e.g. Gonzalez & Reisenegger 2010).

Accurate modelling of neutron star cooling with account of all possible effects is complicated. The cooling can be affected by the presence of free hyperons (e.g. Grigorian, Voskresensky & Maslov 2018; Raduta et al. 2019 and references therein) or deconfined quarks (Wei et al. 2020 and references therein), by emission of axions (e.g. Sedrakian 2019 and references therein), pion or kaon condensation (see Yakovlev et al. 2001 for review and references), and other effects. For simplicity, we assume that the neutron-star matter contains neutrons, protons, electrons, and muons, without hyperons or exotic matter. Also, we restrict ourselves to cooling INSs with not too strong magnetic fields $B \lesssim 10^{14}$ G and not too fast rotation ($\mathcal{P} \gtrsim 10$ ms), neglecting reheating. Then to a good approximation the internal stellar structure is spherically symmetric. It is also reasonable to expect that the temperature distribution is spherically symmetric at sufficiently high densities. In the region of the star where these assumptions are acceptable, the mechanical structure and temperature distribution are determined by a set of differential equations (Richardson et al. 1982), which involve only one spatial coordinate, circumferential radius r. To solve this set of equations, one needs an EoS, which relates pressure P to mass density ρ and temperature T, and a boundary condition, which relates thermal flux to temperature at an outer spherical surface. As a rule, the outer boundary is chosen at such density $\rho_{\rm b}$ that outer layers at $\rho < \rho_{\rm b}$ can be treated as quasi-stationary and the matter at $\rho > \rho_{\rm b}$ is strongly degenerate. Then, the EoS at $\rho > \rho_{\rm b}$ is nearly barotropic (P depends only on ρ but not on T), and the solution of the cooling problem can be greatly simplified: one first solves the hydrostatic equilibrium equations, once and forever, and then uses the stationary hydrostatic structure in the heat transport and thermal balance equations. Many successful neutron star cooling codes work in this way (e.g. Gnedin, Yakovlev & Potekhin 2001; Page 2016). There are also more complicated codes for simulations of neutron-star thermal evolution beyond the approximation of barotropic EoS (e.g. Richardson et al. 1982; Potekhin & Chabrier 2018; Beznogov, Page & Ramirez-Ruiz 2020); they are needed to study hot neutron stars or neutron stars with rapid variations of thermal emission. More complex codes that take into account departures from spherical symmetry are required for studies of rapidly rotating or ultra-magnetized neutron stars (e.g. Chatterjee et al. 2015; Pons & Viganò 2019 and references therein).

2.2 Heat-blanketing envelopes

The above-mentioned quasi-stationary layer is called *heat-blanketing envelope*. Usually, following Gudmundsson, Pethick & Epstein (1983), one sets its bottom at the mass density $\rho_{\rm b} = 10^{10}$ g cm^{-3} (a few hundred meters under the surface). Potekhin & Chabrier (2018) have explicitly demonstrated that this choice provides a good accuracy to the cooling simulations of INSs at ages $t \gtrsim 1$ yr. However, the envelope can be chosen thinner or thicker depending on the problem under consideration.

The composition of the heat blankets is generally unknown. In proto-neutron stars, thermonuclear burning produces the iron group composition near the surface. However, light elements may be supplied by the fallback of matter on to the stellar surface, by accretion from interstellar medium or a companion star and by other processes.

Different chemical elements are separated by rapid sedimentation caused by the strong gravity of neutron stars (Hameury, Heyvaerts & Bonazzola 1983), although thermonuclear processes in the envelopes of accreting neutron stars can instantaneously create complex mixtures (see e.g. Meisel et al. 2018 for review and references). Potekhin, Chabrier & Yakovlev (1997) studied the blanketing envelopes composed, from surface to bottom, of hydrogen, helium, carbon, and iron shells, assuming perfect stratification. More scrupulous envelope treatments include smearing the interfaces between the shells by diffusive mixing of different ions (De Blasio 2000; Chang & Bildsten 2003; Chang, Bildsten & Arras 2010; Beznogov, Potekhin & Yakovlev 2016).

In strong magnetic fields, the heat conduction in the envelopes is anisotropic, so that the temperature varies over the surface (Greenstein & Hartke 1983). However, the total thermal photon luminosity L_γ is only weakly affected by this anisotropy (Potekhin & Yakovlev 2001; Potekhin et al. 2003), except for superstrong fields $B \gtrsim 10^{14}$ G, which appreciably increase the overall heat transparency of the envelope (Potekhin, Urpin & Chabrier 2005; Potekhin & Chabrier 2018).

2.3 Observables

Since the distribution of the surface temperature $T_{\rm s}$ over the neutron-star surface can be non-uniform, it is convenient to introduce the overall effective temperature of the star, $T_{\rm eff}$, defined by

$$4\pi\sigma_{\rm SB} R^2 T_{\rm eff}^4 = L_\gamma = \int F_{\rm s}\, {\rm d}\Sigma = \sigma_{\rm SB} \int T_{\rm s}^4\, {\rm d}\Sigma, \quad (1)$$

where $F_{\rm s}$ is the local flux density at the radiative surface and ${\rm d}\Sigma$ is the surface element. The quantities $T_{\rm s}$, $T_{\rm eff}$, and L_γ refer to a local reference frame at the neutron-star surface. The quantities detected by a distant observer are redshifted (e.g. Thorne 1977):

$$L_\gamma^\infty = L_\gamma(1 - r_{\rm g}/R) = 4\pi\sigma_{\rm SB} \left(T_{\rm eff}^\infty\right)^4 R_\infty^2, \quad (2)$$

$$T_{\rm eff}^\infty = T_{\rm eff}\sqrt{1 - r_{\rm g}/R}, \quad R_\infty = R/\sqrt{1 - r_{\rm g}/R}. \quad (3)$$

2.4 Basic regulators of neutron-star cooling

After a newly born neutron star has passed the initial stage of internal thermal relaxation, which lasts $\sim 10^2$ yr (see Gnedin et al. 2001), it is almost isothermal inside, excluding heat blankets. The isothermality means that the *redshifted* temperature $\widetilde{T} = T(r)\, {\rm e}^{\Phi(r)}$ is independent of r (here, $\Phi(r)$ is a dimensionless metric function, e.g. Misner, Thorne & Wheeler 1973). Subsequent thermal evolution of an INS passes through the neutrino cooling stage and the photon cooling stage, possibly followed by reheating. The time dependence of $\widetilde{T}$ is governed by the heat balance equation:

$$C(\widetilde{T})\, \frac{{\rm d}\widetilde{T}}{{\rm d}t} = -L_\nu^\infty(\widetilde{T}) - L_\gamma^\infty(\widetilde{T}). \quad (4)$$

Here, $C(\widetilde{T})$ and $L_\nu^\infty(\widetilde{T})$ are, respectively, the total heat capacity and the neutrino luminosity of the star, properly integrated over the stellar volume (see e.g. Yakovlev, Levenfish & Haensel 2003).

INSs of age $t \lesssim (0.1 - 0.3)$ Myr cool mainly via neutrino emission ($L_\nu^\infty \gg L_\gamma^\infty$), so that $\widetilde{T}(t)$ is regulated by the ratio $L_\nu^\infty(\widetilde{T})/C(\widetilde{T})$. Older INSs cool via thermal emission of photons from the surface. The neutrino term L_ν becomes negligible in equation (4). At this

stage, the cooling is driven by the ratio $L_\gamma^\infty(\widetilde{T})/C(\widetilde{T})$. At each stage, the dependence $L_\gamma^\infty(\widetilde{T})$, which is provided by a heat blanket model, is needed to obtain the observable photon luminosity. Therefore, using the cooling theory, one can test the heat capacity and the neutrino luminosity of the stellar core, C and L_ν^∞, and heat transparency of the blanketing envelope (determined by composition of plasma as well as by magnetic field strength and geometry).

Microphysics of the crust does not strongly affect the cooling of INSs. It can affect cooling of younger stars (where the crust is non-isothermal) or stars with very strong fields $B \gtrsim 10^{14}$ G (see Potekhin & Chabrier 2018).

The functions $C(\widetilde{T})$ and $L_\nu^\infty(\widetilde{T})$ are mostly determined by properties of superdense matter in the core. One can distinguish the effects of two types.

The effects of first type come from nuclear physics. If the proton fraction (which is strongly model dependent) can reach sufficiently high values in the core, then very fast neutrino cooling via direct Urca processes can proceed (see e.g. Haensel 1995, and references therein). Otherwise the neutrino cooling would be much slower, being mediated mainly by modified Urca processes and neutrino bremsstrahlung in nucleon collisions.

The effects of second type are regulated by superfluidity of neutrons and protons (see Page et al. 2014 for review). In the core, neutron pairing may occur in triplet state, while proton pairing is in singlet state. In the inner crust, dripped neutrons undergo singlet-state pairing. The key theoretical ingredients are critical temperatures $T_{\rm cn}$ and $T_{\rm cp}$ for neutron and proton pairing as functions of ρ, which are related to the so-called superfluid gap functions $\Delta(k_{\rm F})$, where $k_{\rm F}$ is the baryon Fermi wavenumber. Their calculation is very complicated, being affected by numerous delicate effects of in-medium interaction of nucleons (see e.g. Sedrakian & Clark 2019 for review). Modern calculations of the $\Delta(k_{\rm F})$ profiles converge to similar results for the $^1S_0$ pairing of neutrons (Margueron, Sagawa & Hagino 2008; Gandolfi et al. 2009; Ding et al. 2016), which is at work in the crust, but $\Delta(k_{\rm F})$ for the singlet pairing of protons and for triplet pairing of neutrons in the core vary by orders of magnitude depending on employed theoretical model.

Strong pairing of nucleons suppresses their heat capacity and neutrino cooling reactions involving these nucleons (see Yakovlev et al. 2001 for review and practical analytic expressions). When the core temperature becomes much lower than a critical temperature, the suppression can be exponential (almost complete). The suppression of neutrino reactions slows the cooling down, while the suppression of the heat capacity accelerates it. The former effect dominates at the neutrino cooling stage, and the latter becomes most important when the star cools mainly via photon emission. Besides, superfluidity can accelerate the cooling via an additional moderately strong neutrino emission due to Cooper pairing of neutrons. This emission is substantial in the triplet pairing channel when temperature is slightly below $T_{\rm cn}$ (Leinson 2010 and references therein). Therefore, even the direction of superfluidity effects can be different, but all this physics is compressed in the two functions, $C(\widetilde{T})$ and $L_\nu^\infty(\widetilde{T})$. Inferring these functions from the data can give useful information on internal structure of neutron stars.

3 OBSERVATIONS OF COOLING NEUTRON STARS

3.1 General remarks

Only a small fraction of the observed neutron stars is suitable for comparison with the theory of cooling. A vast majority of neutron stars demonstrate intense emission of non-thermal origin. Neutron stars in binary systems are usually surrounded by an accretion disc, whose emission is orders of magnitude more powerful than the thermal emission from the neutron star surface. Non-thermal emission of INSs can be produced by pulsar activity or by other processes in the magnetosphere of the star. A careful analysis is required to extract the thermal component of the observed spectrum.

On the other hand, very old neutron stars, including almost all millisecond pulsars, have already lost their initial heat. Their thermal luminosity is very low, and even if detected, it can be produced by reheating (e.g. Gonzalez & Reisenegger 2010; González-Jiménez, Petrovich & Reisenegger 2015; Yanagi, Nagata & Hamaguchi 2020) or by hot polar caps heated by return currents (e.g. Timokhin & Arons 2013; Salmi et al. 2020).

Another problem is that the age of neutron stars is rarely known with good accuracy. Thus, the 'passive cooling' theory, which neglects reheating, can only be tested against observations of not too old INSs with estimated ages.

To compare neutron-star observations with the cooling theory, one may use either surface temperatures $T_{\rm s}$ or photon luminosities L_γ. Both can be evaluated by spectral analysis, but it is usually difficult to determine them accurately. In empty flat space, the observed flux is inversely proportional to squared distance, while the shape of the spectrum is distance independent. At the first glance, temperature measurements should be preferred since the distance is often poorly known. In reality, however, absorption by interstellar medium appreciably affects both the luminosity and the spectral shape. At typical surface temperatures of cooling neutron stars $T_{\rm s} \sim$ afew $\times$ $(10^5 - 10^6)$ K, thermal flux is emitted mostly in soft X-rays, but a substantial part of the thermal spectrum lies in the extreme ultraviolet range, which is inaccessible to observations because of the strong interstellar absorption. For these reasons, a complete recovery of the spectral shape is a problem even for a neutron star with purely thermal emission. For nearby stars detected in the optical-UV, additional constraints can be obtained from the Rayleigh–Jeans tail of the thermal spectrum (e.g. Shibanov et al. 2005; Kargaltsev & Pavlov 2007; Kaplan et al. 2011).

The analysis of the spectrum can be performed under different hypotheses on the thermal and non-thermal components. Both temperature and luminosity estimates depend on the choice of the emission model. The simplest model is the blackbody (BB) spectrum. More physically motivated models rely on computations of radiative transfer in neutron-star atmospheres or formation of thermal spectrum at a condensed surface (see e.g. Potekhin 2014 for review). Often more than one model can fit equally well the data, without any clear, physically motivated preference. Estimates of the surface temperature, being extracted from observational data by using different models, may vary by a factor of a few. As a rule, they anticorrelate with radius of an equivalent emitting sphere for a distant observer, $R_{\rm eff}^\infty$. Often the model that yields a higher estimate of temperature gives a lower luminosity (mainly because of a smaller bolometric correction). Since the neutron star mass M and physical radius R are rarely known with good accuracy, estimates of redshifted temperature T^∞ and estimates of redshifted photon luminosity L^∞ are usually more robust than non-redshifted ones.

If data contain few photons and/or strong absorption features, the temperature may be poorly constrained by the fit, adding a large statistical error to the systematic one. In such cases L_γ can be determined more accurately than $T_{\rm s}$, especially if the distance to the source is well known. On the other hand, for bright sources with poorly known distances, the observed temperature can be constrained better than the luminosity within a fixed spectral

model, although different models still give different temperature estimates.

Even an accurate estimate of surface temperature may be insufficient for comparison with the cooling theory without a reliable estimate of the luminosity. Indeed, it is L_γ^∞ that enters equation (4). In the ideal case, where T_s is the same at any point on the surface, it equals $T_{\rm eff}$ in equation (2), where, for consistency, one should use the same radius R that is employed in the cooling simulation being compared with the observations. Then, the knowledge of T_s is equivalent to the knowledge of L_γ. However, most neutron stars (including all neutron stars with strong magnetic fields) have anisotropic distribution of temperature over the surface (Section 2.2). Then, a single temperature extracted from observations may be biased upwards because hotter regions contribute more to the detected flux. Accordingly, the effective emitting area is often smaller than $4\pi R^2$, so that $R_{\rm eff}^\infty < R_\infty$. Since the energy balance includes the total photon flux, it would be inconsistent to compare theoretical surface temperature, calculated for the entire emitting surface, with the observational estimate that implies that only a part of the surface emits thermal photons. To restore consistency, L_γ^∞ in equation (4) ought to be corrected by using an appropriate integration area in equation (1).

More sophisticated models allow for a non-uniform temperature distribution. For example, observed spectra are often fitted with models, which include two, or sometimes more, thermal components with different T^∞ and $R_{\rm eff}^\infty$. Usually the hottest component has a small effective radius ($R_{\rm eff}^\infty \ll R_\infty$), which may correspond, for example, to a hotspot on the surface, such as a polar cap of a pulsar heated up by return currents. The hot spots provided by such models usually give minor contribution to the total luminosity. In some cases, however, different fit components have comparable effective radii and give comparable contributions to L^∞. Such a step-like temperature distribution may be an artefact, caused by inadequacy of the assumed spectral model, but it also may mimic a real variation of temperature over the surface.

As will be seen from the comments on observational data in Section 3.3, in some cases the temperature and in other cases the luminosity is better constrained by the data. Sometimes, estimates of both the luminosity and the temperature together help to constrain the parameters of a given neutron star. Thus, it is advisable to take into account the totality of observational data for an analysis of every individual source under study.

3.2 Description of tables

Table 1 gives basic information on middle-aged INSs with registered or reliably constrained thermal radiation that are suitable for comparison with the cooling theory. The key properties of these neutron stars for such a comparison are given in Table 2.

In Table 1, we list the principal identifier of a neutron star, its name or the name of related supernova remnant (SNR), nebula, or stellar association, its spin period $\mathcal{P}$, characteristic dipole field $B_{\rm dip}$, and distance d. Question marks indicate uncertain associations, which are not used in Table 2. The characteristic field is defined by the standard formula (e.g. Manchester & Taylor 1977) $B_{\rm dip} = 3.2 \times 10^{19} \sqrt{\mathcal{P}\dot{\mathcal{P}}}$ G, where $\mathcal{P}$ is in seconds. It gives the field at the magnetic equator of the rotating orthogonal non-relativistic magnetic dipole in vacuo with *canonical neutron star* parameters: mass $M = 1.4\,{\rm M}\odot$, radius $R = 10$ km and moment of inertia $I = 10^{45}$ g cm^2.

Table 2 gives the characteristic age (e.g. Manchester & Taylor 1977) $t_c = \mathcal{P}/(2\dot{\mathcal{P}})$, the age t_* estimated independently of timing, the redshifted bolometric luminosity L^∞ and redshifted surface temperature in energy units $k_{\rm B}T^\infty$. An estimate t_* can be based on proper motion of the star, on physical properties of the associated SNR or surrounding nebula, or, in a few cases, on historical supernova dates (in these cases t_* gives the time of reported spectral measurements). The characteristic ages are usually treated as upper limits. These limits are rather loose: the true ages can sometimes be a factor of 2–3 longer than t_c (for example, for pulsars Vela and J1119–6127; see Section 3.3). Nevertheless, in most cases $t_* < t_c$ (cf. Table 2), sometimes even by orders of magnitude (as for young neutron stars RX J0822.0–4300, 1E 1207.4–5209 and CXOU J185238.6+004020).

If a spectral fit includes both thermal and non-thermal components, only the thermal component of the total luminosity is given. If two or more thermal components are included in the spectral fit, we list the temperature for the cooler one and, over the slash, the hotter one, provided the latter contributes substantially (by more than 15 per cent) to the total flux, and we do the same for the effective radius in the comments. For example, '$k_{\rm B}T^\infty = 154 \pm 4/319^{+13}_{-12}$ eV, $R_{\rm eff}^\infty = 2.21^{+0.08}_{-0.07}/0.37 \pm 0.04$ km' means that one spectral component has been fitted with $k_{\rm B}T^\infty = 154 \pm 4$ eV and $R_{\rm eff}^\infty = 2.21^{+0.08}_{-0.07}$ and the other component with $k_{\rm B}T^\infty = 319^{+13}_{-12}$ eV and $R_{\rm eff}^\infty = 0.37 \pm 0.04$ km, so that each component provides more than 15 per cent of the total luminosity. In such cases, the two components may mimic a real inhomogeneity of temperature distribution over the surface. If the energy contribution of the hotter component is small, it is not listed, because in this case it has a small $R_{\rm eff}^\infty$ and probably represents a hot polar cap heated by reverse currents from the magnetosphere.

The last column of each table indicates references. The reference numbers are marked by letters: 'd' for distance, 'a' for the estimated age t_*, and 's' for spectral analysis. The quantities defined by timing ($\mathcal{P}$, t_c, and $B_{\rm dip}$) mostly rely on the ATNF Pulsar Catalogue (Manchester et al. 2005),[1] to which the reader is addressed for primary references; otherwise we give a reference marked by letter 't' in Table 1. For pulsars with measured parallaxes, we mostly quote distances corrected for the Lutz–Kelker bias from Verbiest et al. (2012), where the reader can find references to original measurements. Some explanations about the listed estimates for each neutron star are given in the comments next.

The objects in the tables are grouped in several classes. Within each class, they are sorted by their mean equinox.

The first class includes central compact objects (CCOs) in SNRs and other thermally emitting INSs (TINSs) without a clear SNR association, which mostly show soft X-ray thermal-like radiation and are not very strongly magnetized ($B_{\rm dip}$ is below 5×10^{11} G or non-determined).

The second and third classes are composed, respectively, of ordinary rotation-powered pulsars with moderately strong magnetic fields $B \sim (10^{12}-10^{13})$ G and high-B pulsars with $B \sim (10^{13}-10^{14})$ G. Such magnetic fields make the temperature distribution over the surface strongly non-uniform, but they only weakly affect thermal luminosity L_γ (see Section 2.2). The first pulsars with clearly measured thermal X-ray spectra, PSR B0656+14, B1055–52, and Geminga, were nicknamed the Three Musketeers by Becker & Trümper (1997).

The fourth class consists of the X-ray emitting neutron stars (XINS). These seven INSs, nicknamed *The Magnificent Seven*, were discovered in the *ROSAT All Sky Survey* (see Haberl 2007; Turolla

[1] https://www.atnf.csiro.au/research/pulsar/psrcat/

Table 1. Isolated middle-aged cooling neutron stars.

no.	Identifier	Association or nickname	$\mathcal{P}$ (s)	$B_{\rm dip}$ (10^{12} G)	Distance (kpc)	Refs.
		I. Weakly magnetized thermal emitters				
1	1E 0102.2–7219	B0102–72.3 in SMC	–	–	62 ± 2	1(d)
2	RX J0822.0–4300	Puppis A	0.113	0.029	2.2 ± 0.3	2(d)
3	CXOU J085201.4–461753	Vela Jr.	–	–	0.77 ± 0.2	3(d)
4	2XMM J104608.7–594306	Homunculus	–	–	2.35 ± 1	4(d)
5	1E 1207.4–5209	G296.5+10.0	0.424	0.098	$2.1^{+1.8}_{-0.8}$	5(t), 6(d)
6	1RXS J141256.0+792204	'Calvera'	0.0592	0.45	∼1–4	7–9(t,d)
7	CXOU J160103.1–513353	G330.2+1.0	–	–	$4.9^{+5}_{-0.3}$	10(d)
8	1WGA J1713.4–3949	G347.3–0.5	–	–	1.3 ± 0.4	11(d)
9	XMMU J172054.5-372652	G350.1–0.3	–	–	$6.1^{+1.3}_{-1.0}$	12(d)
10	XMMU J173203.3–344518	HESS J1731–347	–	–	3.2 ± 0.8	13,14(d)
11	CXOU J181852.0–150213	G015.9+00.2	–	–	$10.0^{+6.7}_{-1.5}$	15(d)
12	CXOU J185238.6+004020	Kes 79	0.105	0.031	$7.1^{+0.4}_{-0.6}$	16(d)
13	CXOU J232327.8+584842	Cas A	–	–	$3.4^{+0.3}_{-0.1}$	17(d)
		II. Ordinary pulsars				
14	PSR J0205+6449	3C 58	0.0657	3.6	2.0 ± 0.3	18(d)
15	PSR J0357+3205	'Morla'	0.444	2.4	0.45 ± 0.05	19(d)
16	PSR J0538+2817	Sim 147	0.143	0.73	$1.47^{+0.42}_{-0.27}$	20(d)
17	CXOU J061705.3+222127	IC 443	$0.25^{+0.35}_{-0.15}$	4–40	1.7 ± 0.3	21(t), 22–24(d)
18	PSR J0633+0632	Collinder 106 (?)	0.297	4.9	$0.9^{+1.1}_{-0.1}$	25(t,d)
19	PSR J0633+1746	'Geminga'	0.237	1.6	$0.25^{+0.23}_{-0.08}$	26(d)
20	PSR B0656+14	Monogem ring	0.385	4.7	0.28 ± 0.03	26(d)
21	PSR B0833–45	Vela	0.0893	3.4	0.28 ± 0.02	26(d)
22	PSR B1055–52	–	0.197	1.1	0.35 ± 0.15	27(d)
23	PSR J1357–6429	HESS J1356–645	0.166	7.8	∼2.5	28(d)
24	PSR B1706–44	G343.1–02.3	0.102	3.1	$2.6^{+0.5}_{-0.6}$	26(d)
25	PSR J1740+1000	–	0.154	1.8	∼1.2–1.4	29(d)
26	PSR J1741–2054	–	0.414	2.7	0.8 ± 0.3	30(d)
27	PSR B1822–09	–	0.769	6.4	0.9–1.9	31(d)
28	PSR B1823–13	–	0.101	2.8	4 ± 1	32(d)
29	PSR J1836+5925	'Next Geminga'	0.173	0.52	∼0.2–0.7	33,34(d)
30	PSR B1951+32	CTB 80	0.0395	0.49	2.4 ± 0.2	35(d)
31	PSR J1957+5033	–	0.375	1.6	∼0.1–0.8	36(t,d), 37(d)
32	PSR J2021+3651	–	0.104	3.2	$1.8^{+1.7}_{-1.4}$	38(d)
33	PSR B2334+61	G114.3+00.3	0.495	9.9	∼0.7	39(d)
		III. High-B pulsars				
34	PSR J0726–2612	–	3.442	32	$1.0^{+1.4}_{-0.7}$	40,41(d)
35	PSR J1119–6127	G292.2–00.5	0.408	41	8.4 ± 0.4	42(d)
36	PSR B1509–58	–	0.151	15	5.2 ± 1.4	43(d)
37	PSR J1718–3718	–	3.379	75	4.5–10	44(d)
38	PSR J1819–1458	–	4.263	50	3.6 ± 0.9	45(d)
		IV. The Magnificent Seven				
39	RX J0420.0–5022	–	3.453	9.9	0.325–0.345	46(t), 47(d)
40	RX J0720.4–3125	–	16.782	24	0.286^{+27}_{-23}	48(t), 47,49(d)
41	RX J0806.4-4123	–	11.370	26	0.235–0.250	47(d)
42	RX J1308.6+2127	–	10.312	34	$0.38^{+0.02}_{-0.03}$	50,51(d)
43	RX J1605.3+3249	–	–	–	0.09–0.4	52,53(t), 47,52–55(d)
44	RX J1856.5–3754	Upper Scorpius	7.055	15	$0.123^{+0.011}_{-0.015}$	56(t), 57(d)
45	RX J2143.0+0654	–	9.428	200	0.390–0.430	58(t), 47(d)
		V. Neutron stars with upper limits on thermal emission				
46	PSR J0007+7303	CTA 1	0.316	1.1	1.4 ± 0.3	59(d)
47	PSR B0531+21	Crab	0.0334	3.8	$2.0^{+0.7}_{-0.6}$	60(d)
48	PSR B1727–47	RCW 114	0.830	12	0.5–0.8	61,62(d)
49	PSR J2043+2740	Cygnus loop (?)	0.0961	0.35	1.5–1.8	63,64(d)
50	PSR B2224+65	Guitar	0.683	2.6	$0.83^{+0.17}_{-0.10}$	65(d)
		VI. Middle-aged pulsars with measured thermal emission of hot spots				
51	PSR B0114+58	–	0.101	0.78	1.8 ± 0.6	66(d)
52	PSR B0943+10	–	1.098	2.0	0.63–0.89	67(d)
53	PSR B1133+16	–	1.188	2.1	0.35 ± 0.02	26(d)

Table 1 – *continued*

no.	Identifier	Association or nickname	$\mathcal{P}$ (s)	$B_{\rm dip}$ (10^{12} G)	Distance (kpc)	Refs.
54	PSR J1154-6250	–	0.282	0.40	1.36–1.77	68(d)
55	PSR B1929+10	–	0.227	0.52	$0.31^{+0.09}_{-0.05}$	26(d)

Note. References: 1. Graczyk et al. (2014); 2. Reynoso et al. (2003); 3. Allen et al. (2015); 4. Smith (2006); 5. Halpern & Gotthelf (2015); 6. Giacani et al. (2000); 7. Halpern et al. (2013); 8. Zane et al. (2011); 9. Shibanov et al. (2016); 10. McClure-Griffiths et al. (2001); 11. Cassam-Chenaï et al. (2004); 12. This work (spectral fit); 13. Klochkov et al. (2015); 14. Maxted et al. (2018); 15. Sasaki et al. (2018); 16. Giacani et al. (2009); 17. Reed et al. (1995); 18. Kothes (2013); 19. Kirichenko et al. (2014); 20. Ng et al. (2007); 21. Swartz et al. (2015); 22. Fesen (1984); 23. Welsh & Sallmen (2003); 24. Kochanek, Auchettl & Belczynski (2019); 25. Danilenko et al. (2020); 26. Verbiest et al. (2012); 27. Mignani et al. (2010); 28. Zavlin (2007); 29. Kargaltsev et al. (2012); 30. Karpova et al. (2014); 31. Hermsen et al. (2017); 32. Pavlov et al. (2008); 33. Abdo et al. (2010); 34. Arumugasamy (2015); 35. Strom & Stappers (2000); 36. Marelli et al. (2015); 37. Zyuzin et al. (in preparation); 38. Kirichenko et al. (2015); 39. Yar-Uyaniker et al. (2004); 40. Speagle et al. (2011); 41. Rigoselli et al. (2019a); 42. Caswell et al. (2004); 43. Gaensler et al. (1999); 44. Zhu et al. (2011); 45. Miller et al. (2013); 46. Kaplan & van Kerkwijk (2011); 47. Posselt et al. (2007); 48. Hambaryan et al. (2017); 49. Tetzlaff et al. (2011); 50. Motch et al. (2009); 51. Hambaryan et al. (2011); 52. Pires et al. (2019); 53. Malacaria et al. (2019); 54.Motch et al. (2005); 55. Tetzlaff et al. (2012); 56. van Kerkwijk & Kaplan (2008); 57. Walter et al. (2010); 58. Kaplan & van Kerkwijk (2009); 59. Pineault et al. (1993); 60. Trimble (1973); 61. Shternin et al. (2019); 62. Zyuzin et al. (in preparation); 63. Becker et al. (2004); 64. Testa et al. (2018); 65. Deller et al. (2019); 66. Rigoselli & Mereghetti (2018); 67. Rigoselli et al. (2019b); 68. Igoshev et al. (2018).

2009; Kaplan & van Kerkwijk 2009, for reviews). Their soft X-ray radiation can be mostly thermal, but unlike CCOs and TINSs, they have very strong magnetic fields, similar to those of the high-B pulsars.

Next, we present a bunch of not too old pulsars with upper bounds on their thermal luminosity, which may be useful for constraining cooling predictions.

Finally, we list a group of pulsars whose effective thermally emitting areas are very small ($R^{\infty}_{\rm eff} \lesssim 0.5$ km), suggesting that their thermal radiation may originate mostly in the polar caps. These estimates may be useful because the registered hot-cap luminosity can be regarded as an upper bound on the total thermal luminosity. However, these upper bounds are not absolute because a soft thermal emission from the entire surface might escape detection. For example, Rigoselli & Mereghetti (2018) derived 3σ upper bounds of 3.2×10^{28} and 2.4×10^{29} erg s^{-1} on the bolometric luminosities of a possible thermal component with $k_{\rm B}T^{\infty}$ between 50 and 2 keV for the pulsars B0628–28 and B0919+06, respectively. Meanwhile, for a neutron star with typical $R_{\infty} \sim 15$ km, thermal radiation with $k_{\rm B}T^{\infty} \sim 25$ eV (below the formal applicability range of these bounds) would correspond to $L^{\infty} \sim 10^{31}$ erg s^{-1} (well above these limits). On the other hand, there are a number of thermal-like spectra of pulsars, which could be interpreted as produced by hot spots, while fitted with the BB spectrum, because of rather low inferred $R^{\infty}_{\rm eff}$ and high T^{∞}, whereas the interpretation by a thermal emission from the entire surface becomes possible when an atmosphere model is applied.

The ages and observational estimates of thermal luminosity or surface temperature from Table 2 are compared with theoretical cooling curves in Section 4.

3.3 Comments on individual objects

The objects in the list next are numbered in the same order as in Tables 1 and 2.

3.3.1 Weakly magnetized thermally emitting neutron stars

1. *1E 0102.2–7219* belongs to an SNR, which was revealed in X-rays by the *Einstein* observatory. Its location in the Small Magellanic Cloud fixes its distance to $d = 62 \pm 2$ kpc (Graczyk et al. 2014 and references therein). Its age was estimated in a number of papers (see Xi et al. 2019 and references therein). Vogt et al. (2018) discovered the respective CCO in the data of the *Chandra* X-ray observatory. Hebbar, Heinke & Ho (2020) confirmed this detection and performed a spectral analysis using archival *Chandra* observations. We adopt their preferred result ($T_{\rm s} = 3.0^{+0.5}_{-0.4}$ MK, $R^{\infty}_{\rm eff}/R_{\infty} = 0.5^{+0.5}_{-0.2}$, $N_{\rm H} = 9^{=12}_{-7} \times 10^{21}$ cm^{-2}, $L^{\infty} = 1.1^{+1.6}_{-0.5} \times 10^{34}$ erg s^{-1}), which was obtained with the NSMAX spectral model[2] of an atmosphere composed of partially ionized carbon at magnetic field $B = 10^{12}$ G on a neutron star with fixed $M = 1.4\,{\rm M}_{\odot}$ and $R = 12$ km with free normalization of the point source and background fluxes. This model provides the only satisfactory one-component spectral fit. Other statistically acceptable fits include multiple spectral components and suggest temperatures and luminosities varying in substantially wider ranges. Besides, the authors warn that the high contribution from the background makes the statistical confidence of different fits somewhat uncertain.

2. *RX J0822.0–4300 (PSR J0821–4300)* is a CCO in the SNR Puppis A (G260.4–03.4). Its age was estimated from the proper motion measurements (Becker et al. 2012). The two BB (2BB) fit to the spectrum at fixed distance $d = 2.2$ kpc gives $k_{\rm B}T^{\infty} = 265 \pm 15/455 \pm 20$ eV with $R^{\infty}_{\rm eff}$ varying from 2.27/0.53 to 2.04/0.65 km between the 'soft' and 'hard' phases of the pulse profile (De Luca et al. 2012). The sum of the cooler and hotter components thus varies from $L^{\infty} = (4.8^{+1.1}_{-0.9}) \times 10^{33}$ erg s^{-1} in the 'soft' phase to $L^{\infty} = 5.0^{+1.1}_{-0.9} \times 10^{33}$ erg s^{-1} in the 'hard' phase of the pulse.

3. *CXOU J085201.4–461753* is a CCO in the SNR Vela Jr. (G266.2–1.2). Its age and distance were estimated from an expansion rate and a hydrodynamic analysis (Allen et al. 2015). Using the NSX model of the carbon atmosphere, Danilenko et al. (2015) showed that the X-ray spectrum of this CCO agrees with thermal radiation of a neutron star at $T^{\infty} = 1.3$ MK. An alternative BB fit implies a small emitting area, which is difficult to agree with the tight constraint on the pulsed fraction < 3 per cent.

4. *2XMM J104608.7–594306*. This neutron star, possibly in the Homunculus nebula around η Carina, has purely thermal X-ray spectrum. Its age estimate is based on a proposed association of a nearby star with its progenitor (Pires et al. 2015). Having performed

[2]The named atmosphere models (NSMAX by Ho, Potekhin & Chabrier 2008; NSA by Zavlin, Pavlov & Shibanov 1996; NSMAXG by Ho 2014; NSX by Ho & Heinke 2009; CARBATM by Suleimanov et al. 2014; TBABS by Wilms, Allen & McCray 2000) are from the XSPEC package (Arnaud 1996) at https://heasarc.gsfc.nasa.gov/docs/xanadu/xspec/.

Table 2. Ages and thermal radiation of cooling neutron stars.

no.	Short name	t_c (kyr)	t_* (kyr)	L^∞ (10^{32} erg s^{-1})	$k_B T^\infty$ (eV)	Refs.
			I. Weakly magnetized thermal emitters			
1	1E 0102	–	2.1 ± 0.6	110^{+160}_{-50}	210^{+40}_{-30}	1(a), 2(s)
2	Puppis A NS	2.54×10^5	4.45 ± 0.75	50 ± 11	$276 \pm 15/455 \pm 20$	3(a), 4(s)
3	Vela Jr. NS	–	2.1–5.4	20 ± 10	90 ± 10	5(a), 6(s)
4	J1046	–	11–30	0.8–6	40–70	7(a,s)
5	1E 1207	3.01×10^5	7^{+14}_{-5}	$13.1^{+4.9}_{-1.6}$	90–250	8(a), 9(s)
6	Calvera	285	–	2–50	65–210	10,11(s)
7	J1601	–	0.8 ± 0.2	58 ± 2	118 ± 1	12(a), 13(s)
8	J1713	–	1.608	∼20–120	138 ± 1	14(a), 15(s)
9	J1720	–	0.6–1.2	150–270	161 ± 9	16(a), 15(s)
10	J1732	–	2–6	174^{+19}_{-39}	153^{+4}_{-2}	17(a), 18(s)
11	J1818	–	$3.4^{+2.6}_{-0.7}$	84^{+68}_{-42}	130 ± 20	19(a), 20(s)
12	Kes 79 NS	1.92×10^5	$6.0^{+1.8}_{-2.8}$	104^{+24}_{-20}	133 ± 1	21(a), 22(s)
13	Cas A NS	–	0.320–0.338	61–94	123–185	23(a), 24–26(s)
			II. Ordinary pulsars			
14	J0205	5.37	0.819	$1.9^{+1.5}_{-1.1}$	49^{+5}_{-6}	27,28(a), 15(s)
15	Morla	541	200–1300	$0.15^{+0.25}_{-0.11}$	36^{+9}_{-6}	29(a,s)
16	J0538	620	40 ± 20	$10.9^{+2.7}_{-4.6}$	91 ± 5	30(a), 31(a,s)
17	J0617	10–100	∼30	2.6 ± 0.1	$58.4^{+0.6}_{-0.4}$	32(a), 33(s)
18	J0633	59.2	–	$1.5^{+2.5}_{-0.9}$	53 ± 4	34(s)
19	Geminga	342	–	$0.88^{+0.21}_{-0.39}$	42 ± 2	35,36(s)
20	B0656	111	–	$6.7^{+2.1}_{-1.5}$	$64 \pm 4/123^{+6}_{-5}$	37(s)
21	Vela pulsar	11.3	17–23	4.24 ± 0.12	57^{+3}_{-1}	38(a), 39(s)
22	B1055	535	–	$1.0^{+1.0}_{-0.7}$	68 ± 3	40(s)
23	J1357	7.31	–	3.6 ± 0.7	64 ± 4	41,42(s)
24	B1706	17.5	–	$7.1^{+1.6}_{-6.5}$	71^{+140}_{-30}	43(s)
25	J1740	114	–	$1.9^{+3.1}_{-1.0}$	67 ± 11	44(s)
26	J1741	386	–	$3.1^{+1.4}_{-1.0}$	60 ± 2	45(s)
27	B1822	233	–	$0.26^{+0.12}_{-0.09}$	83 ± 4	46(s)
28	B1823	21.4	–	4.5 ± 0.9	97^{+4}_{-5}	47(s)
29	Next Geminga	1.83×10^3	–	$0.014^{+0.016}_{-0.006}$	$15.9^{+3.3}_{-2.2}$	48(s)
30	B1951	107	64 ± 18	$1.8^{+3.0}_{-1.1}$	130 ± 20	49(a), 50(s)
31	J1957	870	–	0.012–0.11	∼13–25	51(s)
32	J2021	17.2	–	5^{+3}_{-2}	63^{+6}_{-5}	52(s)
33	B2334	40.6	∼7.7	0.47 ± 0.35	38^{+6}_{-9}	53(a), 54(s)
			III. High-B pulsars			
34	J0726	186	–	$4.0^{+4.4}_{-1.0}$	74^{+6}_{-11}	55(s)
35	J1119	1.61	4.2–7.1	19^{+19}_{-8}	∼80–210	56(a), 57(s)
36	B1509	1.56	–	90 ± 20	142^{+7}_{-9}	58(s)
37	J1718	33.2	–	4^{+5}_{-2}	57–200	59(s)
38	J1819	120	–	30^{+50}_{-22}	138^{+3}_{-25}	60(s)
			IV. The Magnificent Seven			
39	J0420	1.98×10^3	–	0.06 ± 0.02	45.0 ± 2.6	61,62(s)
40	J0720	1.90×10^3	850 ± 150	$1.9^{+1.3}_{-0.8}$	90–100	63(a), 64,65(s)
41	J0806	3.24×10^3	–	0.16–0.25	∼90–110	61,62(s)
42	J1308	1.46×10^3	550 ± 250	$3.3^{+0.5}_{-0.7}$	∼50–90	66(a), 67(a,s)
43	J1605	–	440^{+70}_{-60}	0.07–5	35–120	68(a), 69,70(s)
44	J1856	3.76×10^3	420 ± 80	0.5–0.8	36–63	71(a), 72 –74(s)
45	J2143	3.7×10^3	–	0.5–1.7	40/100	75(s)
			V. Upper limits			
46	J0007	13.9	≈9.2	<0.3	<200	76(a), 77(s)
47	Crab pulsar	1.26	0.954	<300	<180	78(a), 79(s)
48	B1727	80.5	50 ± 10	<0.35	<33	80(a), 81(s)
49	J2043	1.20×10^3	–	<0.4	<80	82–84(s)
50	Guitar pulsar	1.13×10^3	–	<1.7	<110	85(s)
			VI. Hot spots			
51	B0114	275	–	0.044 ± 0.003	170 ± 20	86(s)
52	B0943	4.98×10^3	–	0.001–0.005	$82^{+3}_{-9} - (\sim 220)$	87(s)

Table 2 – *continued*

no.	Short name	t_c (kyr)	t_* (kyr)	L^∞ (10^{32} erg s^{-1})	k_BT^∞ (eV)	Refs.
53	B1133	5.04×10^3	–	$0.0003^{+0.0017}_{-0.0002}$	190^{+40}_{-30}	88(s)
54	J1154	7.99×10^3	–	0.017 ± 0.05	210 ± 40	89(s)
55	B1929	3.11×10^3	–	$0.0084^{+0.0034}_{-0.0022}$	300^{+20}_{-30}	90(s)

Note. References: 1. Xi et al. (2019); 2. Hebbar et al. (2020); 3. Becker et al. (2012); 4. De Luca et al. (2012); 5. Allen et al. (2015); 6. Danilenko et al. (2015); 7. Pires et al. (2015); 8. Roger et al. (1988); 9. Mereghetti et al. (2002); 10. Shibanov et al. (2016); 11. Bogdanov et al. (2019); 12. Borkowski et al. (2018); 13. Doroshenko et al. (2018); 14. Cassam-Chenaï et al. (2004); 15. This work; 16. Lovchinsky et al. (2011); 17. Cui et al. (2016); 18. Klochkov et al. (2015); 19. Sasaki et al. (2018); 20. Klochkov et al. (2016); 21. Sun et al. (2004); 22. Bogdanov (2014); 23. Flamsteed (1680), Ashworth (1980); 24. Heinke & Ho (2010); 25. Posselt & Pavlov (2018); 26. Wijngaarden et al. (2019); 27. Stephenson (1971); 28. Kothes (2013); 29. Kirichenko et al. (2014); 30. Kramer et al. (2003); 31. Ng et al. (2007); 32. Chevalier (1999); 33. Swartz et al. (2015); 34. Danilenko et al. (2020); 35. De Luca et al. (2005); 36. Mori et al. (2014); 37. Arumugasamy et al. (2018); 38. Aschenbach (2002); 39. Ofengeim & Zyuzin (2018); 40. Mignani et al. (2010); 41. Zavlin (2007); 42. Chang et al. (2012); 43. McGowan et al. (2004); 44. Kargaltsev et al. (2012); 45. Karpova et al. (2014); 46. Hermsen et al. (2017); 47. Pavlov et al. (2008); 48. Arumugasamy (2015); 49. Migliazzo et al. (2002); 50. Li et al. (2005); 51. Zyuzin et al. (in preparation); 52. Kirichenko et al. (2015); 53. Yar-Uyaniker et al. (2004); 54. McGowan et al. (2006); 55. Rigoselli et al. (2019a); 56. Kumar et al. (2012); 57. Ng et al. (2012); 58. Hu et al. (2017); 59. Zhu et al. (2011); 60. Miller et al. (2013); 61. Haberl et al. (2004); 62. Kaplan & van Kerkwijk (2009); 63. Tetzlaff et al. (2011); 64. Hohle et al. (2012a); 65. Hambaryan et al. (2017); 66. Motch et al. (2009); 67. Hambaryan et al. (2011); 68. Tetzlaff et al. (2012); 69. Pires et al. (2019); 70. Malacaria et al. (2019); 71. Mignani et al. (2013); 72. Ho et al. (2007); 73. Sartore et al. (2012); 74. Yoneyama et al. (2017); 75. Schwope et al. (2009); 76. Martín et al. (2016); 77. Caraveo et al. (2010); 78. Stephenson & Green (2003); 79. Weisskopf et al. (2011); 80. Shternin et al. (2019); 81. Zyuzin et al. (in preparation); 82. Becker et al. (2004); 83. Zavlin & Pavlov (2004); 84. Zavlin (2009); 85. Hui & Becker (2007); 86. Rigoselli & Mereghetti (2018); 87. Rigoselli et al. (2019b); 88. Szary et al. (2017); 89. Igoshev et al. (2018); 90. Misanovic et al. (2008).

an analysis based on different spectral models, Pires et al. (2015) concluded that the spectrum can only be well fitted with including at least one absorption line at energy 1.35 keV. If interpreted as a redshifted electron cyclotron line, it implies $B \sim 1.5 \times 10^{11}$ G. In this case, $T_s = (6–10) \times 10^5$ K and the X-ray luminosity $L_X = (1.1–7.4) \times 10^{32}$ erg s^{-1}. Taking into account the gravitational redshift and the bolometric correction, this translates into $k_BT^\infty = 40–70$ eV and $L^\infty = (0.8–6) \times 10^{32}$ erg s^{-1}.

5. *1E 1207.4–5209 (PSR J1210–5209)* is a CCO in the SNR G296.5+10.0. The estimate and uncertainties of the luminosity are obtained by comparison of three fitting models at fixed $d = 2$ kpc in table 1 of Mereghetti et al. (2002). The corresponding effective radius is $R^\infty_{\rm eff} = 2.1 \pm 0.3$ km. Roger et al. (1988) give $t_* \sim 7$ kyr with an uncertainty up to a factor of 3.

6. *1RXS J141256.0+792204 (PSR J1412+7922, RX J1412.9+7922)*. This enigmatic TINS was initially considered as a possible addition to the 'Magnificent Seven' and was dubbed 'Calvera' (Rutledge, Fox & Shevchuk 2008). However, subsequent observations suggest that its properties are closer to the CCOs. Halpern, Bogdanov & Gotthelf (2013) characterized Calvera as an 'orphaned CCO,' whose magnetic field is emerging through supernova debris. They tried to estimate the distance and age of Calvera and concluded that both remain uncertain by an order of magnitude. Zane et al. (2011) performed the first detailed analysis of its spectrum. Among numerous fits tried by the authors, only those with the interstellar hydrogen column density N_H fixed to the Galactic value 2.7×10^{20} cm^{-2} gave an acceptable reduced chi-square statistic χ^2_ν and a reasonable distance (other fits gave distances down to 175 pc, too large N_H and tiny emitting area). A fit with a two-temperature atmosphere model (2NSA) gave $k_BT^\infty = 67^{+7}_{-12}$ eV/150^{+12}_{-20} eV, with radius of the cold component fixed at the realistic value $R = 12$ km. This fit gave $L^\infty \sim 6 \times 10^{32}$ erg s^{-1} at $d \approx 1.55$ kpc. Other acceptable fits indicated d in the range from $\sim$1 kpc to $\approx$2.25 kpc. The values of the unabsorbed flux for various statistically acceptable fits implied L^∞ ranging from 5.5×10^{32} to 9.2×10^{32} erg s^{-1}, assuming $d = 2$ kpc. Shibanov et al. (2016) fitted the *XMM–Newton* and *Chandra* data using NSMAX models of magnetized hydrogen atmospheres covering the entire surface, assuming a centred dipole field and the ensuing temperature distribution. They found that an additional absorption feature at energy $E_{\rm abs} = 740 \pm 30$ eV improved the fit. In this case, the best-fitting model yields $T^\infty = 1.18 \pm 0.05$ MK. The resulting normalization (the effective emitting radius) can be reconciled with $R = 12$ km (assumed in the NSMAX model) at $d \sim 4$ kpc. The corresponding luminosity is $L^\infty = (3.0 \pm 0.5) \times 10^{33}$ erg s^{-1}. Other fits, performed for different data sets with or without involving the absorption, are only slightly worse statistically. They yield T^∞ from 0.79 ± 0.03 MK to $1.34^{+0.01}_{-0.02}$ MK, corresponding to $L^\infty \sim 5 \times (10^{32} - 10^{33})$ erg s^{-1}. Bogdanov et al. (2019) have performed an analysis of the spectrum obtained with *NICER*. They fixed $d = 2$ kpc and obtained $k_BT^\infty = 205 \pm 3$ eV, $R^\infty_{\rm eff} = 1.01^{+0.04}_{-0.03}$ km ($L^\infty = 2.33^{+0.29}_{-0.14} \times 10^{32}$ erg s^{-1}) for a BB plus power-law (BB+PL) fit with an absorption at $E_{\rm abs} = 780 \pm 20$ eV. An alternative fit including a Gaussian absorption at $E_{\rm abs} = 760 \pm 10$ eV and two BB components (the G2BB fit) gives $k_BT^\infty = 154 \pm 4/319^{+13}_{-12}$ eV, $R^\infty_{\rm eff} = 2.21^{+0.08}_{-0.07}/0.37 \pm 0.04$ km, totalling to $L^\infty = (5.4 \pm 0.6) \times 10^{32}$ erg s^{-1}. The ranges of L^∞ and T^∞ in Table 2 cover the results obtained by Bogdanov et al. (2019) and by Shibanov et al. (2016) for the different instruments.

7. *CXOU J160103.1–513353* is a CCO in the SNR G330.2+1.0. Proper motion of the SNR fragments indicates an age of 0.8–1 kyr, if one neglects deceleration; because of deceleration the actual age should be smaller (Borkowski et al. 2018; Williams et al. 2018). McClure-Griffiths et al. (2001) derived the minimum distance to this SNR of $d = 4.9 \pm 0.3$ kpc from the observed velocities in the absorption spectrum; a hypothetical maximum distance is $d < 9.9$ kpc. The X-ray spectrum of the CCO is well described with either single-component carbon or two-component hydrogen atmosphere models (Doroshenko, Suleimanov & Santangelo 2018). In the latter case, the observed spectrum is dominated by the emission from a hot component with a temperature $\sim$3.9 MK, corresponding to the emission from a hotspot occupying 1 per cent of the stellar surface, assuming a neutron star with $M = 1.5\,M_\odot$ and $R = 12$ km at $d \sim 5$ kpc. The carbon atmosphere model yields more plausible results. Using absorbed CARBATM model with fixed $d = 4.9$ kpc, $M = 1.5M_\odot$ and $R = 12$ km, Doroshenko et al. (2018) obtained non-redshifted temperature $T_s = 1.73 \pm 0.01$ MK.

8. *1WGA J1713.4–3949* is a compact X-ray source, which was suggested to be a neutron star associated with the SNR G347.3–0.5 (Slane et al. 1999; Lazendic et al. 2003; Cassam-Chenaï et al. 2004). Alternatively, 1WGA J1713.4–3949 may be a background extra-Galactic source (Slane et al. 1999). Radio pulsar PSR J1713–3945 at the centre of the SNR G347.3–0.5 is unrelated to 1WGA J1713.4–3949 (Lazendic et al. 2003) and thus could be considered as an alternative association candidate. However, the large characteristic age $t_c = 1.1$ Myr of PSR J1713–3945 and its dispersion-measure distance estimate of 4.3 kpc make it unlikely to be associated with the SNR G347.3–0.5 (Lazendic et al. 2003). Location of the SNR G347.3–0.5 probably coincides with the historical supernova SN 393 (Wang, Qu & Chen 1997), giving the age around 1608 yr at the time of the *XMM–Newton* spectral observations. The SNR distance is $d = 1.3 \pm 0.4$ kpc, as argued by Cassam-Chenaï et al. (2004) and corroborated, e.g. by Moriguchi et al. (2005) and Fukui et al. (2012). The distance ∼1 kpc is also compatible with $t_* \sim 1.6$ kyr (Maxted et al. 2013). A BB+PL fit to the X-ray spectrum ($\chi^2_\nu = 1.06$) gives $k_B T^\infty = 400 \pm 20$ eV, $R^\infty_{\rm eff} = 0.35 d_{\rm kpc}$ and $L^\infty = (3.2 \pm 0.4) \times 10^{32} d^2_{\rm kpc}$ erg s^{-1}, where $d_{\rm kpc} \equiv d/1$ kpc (Cassam-Chenaï et al. 2004). This is compatible with the hotspot emission, but the lack of pulsations casts doubt on such interpretation. The 2BB fit is slightly better ($\chi^2_\nu = 1.03$); it gives $k_B T^\infty = 320^{+20}_{-30}$ eV, $L^\infty = (4.4 \pm 0.4) \times 10^{32} d^2_{\rm kpc}$ erg s^{-1} for the cold component and $k_B T^\infty = 570^{+70}_{-50}$ eV, $L^\infty = 1.7^{+0.6}_{-0.3} \times 10^{32} d^2_{\rm kpc}$ erg s^{-1} for the hot component, but again with small effective radii ∼0.1–0.6 km.

Our analysis of archival *XMM–Newton* EPIC-pn data (OBsID 0740830201), using the TBABS × NSX model with fixed $M = 1.4 M_\odot$ and $R = 13$ km, gives $T^\infty = 1.60 \pm 0.05$ MK, $L^\infty = (1.1 \pm 0.1) \times 10^{34}$ erg s^{-1} and $d = 3.20^{+0.28}_{-0.26}$ kpc (at 95 per cent confidence), inconsistent with the distance to G347.3–0.5. The same fit with fixed $d = 1$ kpc requires normalization of 0.2 (i.e. $R^\infty_{\rm eff} \approx 7$ km), which gives $L^\infty \sim 2 \times 10^{33}$ erg s^{-1}.

9. *XMMU J172054.5–372652* is a compact thermal X-ray source, probably associated with the SNR G350.1–0.3, as suggested by Gaensler et al. (2008), who also proposed that the SNR G350.1–0.3 is probably interacting with a molecular cloud at $d \approx 4.5$ kpc. Lovchinsky et al. (2011) showed that the SNR G350.1–0.3 is in the free expansion stage and calculated an age of 600–1200 yr.

We used archival *Chandra* (OBsID 10102, 14806) data and fitted the spectrum with the TBABS × NSX model in the range 0.5–6 keV. We fixed neutron star mass $M = 1.4\,M_\odot$, radius $R = 13$ km, and distance $d = 4.5$ kpc. The non-redshifted temperature is $T_s = 2.06 \pm 0.02$ MK ($T^\infty = 1.71 \pm 0.02$ MK; $L^\infty = (1.51 \pm 0.07) \times 10^{34}$ erg s^{-1}). Letting distance to vary, we obtained $d = 6.1^{+2.6}_{-1.9}$ kpc and $T^\infty = 1.87^{+0.21}_{-0.20}$ MK (95 per cent confidence). In each case, we got $\chi^2_\nu = 1.03$ (356 and 355 degrees of freedom, respectively).

10. *XMMU J173203.3–344518* is a CCO in the SNR HESS J1731–347 (G353.6–00.7). For this X-ray source, two likely distance values used to be considered, $d \sim 3.2$ or 4.5 kpc (H. E. S. S. Collaboration 2011). The spectral analysis by Klochkov et al. (2015) gave an acceptable neutron star radius $R = 12.4^{+0.9}_{-2.2}$ km only for $d \sim 3.2$ kpc and only for the carbon atmosphere model. The analysis suggested the mass $M = 1.55^{+0.28}_{-0.24}\,M_\odot$. Later, the distance $d \approx 3.2$ kpc was confirmed by Maxted et al. (2018), based on an analysis of photoabsorption by neutral hydrogen. Klochkov et al. (2015) adopted the age of this neutron star from Tian et al. (2008), who had suggested association of the SNR with molecular gas connected with the H II region G353.43–00.37 and calculated a radiative SNR age of 27 kyr. For that age, the obtained $k_B T^\infty = 153^{+4}_{-2}$ eV would be too high to be explained by the ordinary neutron star cooling theory. Klochkov et al. (2015) discussed possible cooling scenarios including unusual baryon superfluidity to explain this oddity. Later, however, it was shown that, at $d = 3.2$ kpc, the SNR should be much younger, $t \sim 2$–6 kyr (Acero et al. 2015; Cui, Pühlhofer & Santangelo 2016; Maxted et al. 2018), which can be consistent with less unusual cooling scenarios.

11. *CXOU J181852.0–150213* is a CCO in the SNR G15.9+00.2. The quoted luminosity and temperature correspond to the spectral fit with the carbon atmosphere model for fixed $M = 1.5\,M_\odot$ and $R = 12$ km, with unfixed N_H and d (Klochkov et al. 2016). This fit gives $d = 10^{+9}_{-5}$ kpc, compatible with $d = 8.5$–16 kpc derived by Sasaki et al. (2018) from the SNR properties (other fits give much larger d and therefore should be rejected). The age is estimated as $t_* = (3.4 \pm 0.2)\,(d/10\ {\rm kpc})$ kyr (Sasaki et al. 2018).

12. *CXOU J185238.6+004020 (PSR J1852+0040)* is a CCO in the SNR Kes 79 (G033.6+00.1). The age estimate is based the SNR properties (Sun et al. 2004). The luminosity and temperature are quoted from Bogdanov (2014), based on the CARBATM model and assuming $d = 7.1$ kpc, $M = 1.4\,M_\odot$, and $R = 9$, 12, or 14 km. The effective emitting area was allowed to vary and proved to be of the order of the physical surface area (within a factor of ∼0.8–1.9). The 2BB and NSMAX fits give less plausible results (much smaller emitting areas).

13. *CXOU J232327.8+584842*, aka Cas A NS, is a CCO in the SNR Cas A (G111.7–02.1), which was produced by supernova observed by Flamsteed on 1680 August 16 (Ashworth 1980; this attribution is supported by the age of the SNR, derived from observations by Fesen et al. 2006). Historically, it is the first neutron star whose spectrum has been successfully fitted by the carbon atmosphere model (Ho & Heinke 2009). Its temperature and luminosity obtained using this model are rapidly decreasing over the time of its observations by the *Chandra* X-ray observatory since 2000 (Heinke & Ho 2010). The decrease of T^∞ by ∼4–5 per cent from 2000 to 2018 (see table B1 in Wijngaarden et al. 2019) is at odds with theoretical cooling models. It has been tentatively explained by neutrino emission in the Cooper pairing processes (Section 2.4), assuming that the internal temperature has passed the critical value for the onset of neutron superfluidity a few decades ago (Shternin et al. 2011; Page et al. 2011; see also Ho et al. 2015 and references therein). However, a revision of the Cooper pairing-related emission rate by Leinson (2010) makes the theoretical cooling rate anyway incompatible with the observed one (Leinson 2016; Potekhin & Chabrier 2018). Posselt et al. (2013) suggested that the observed decline may be not intrinsic to the neutron star, and put forward alternative hypotheses for its explanation. According to Posselt & Pavlov (2018), an assumption that the column density can vary between the observations makes the observed flux variation statistically insignificant. The analysis of observations in *Chandra* ACIS Graded mode (e.g. Heinke & Ho 2010; Wijngaarden et al. 2019) gives noticeably higher T^∞ and systematically quicker fading than those in *Chandra* ACIS subarray mode (Posselt et al. 2013; Posselt & Pavlov 2018); this difference has not been explained by the time of this writing. The ranges of L^∞ and T^∞ in Table 2 accommodate different estimates from the above-cited works over the observation dates from 2000 to 2018.

3.3.2 *Moderately magnetized middle-aged pulsars*

14. *PSR J0205+6449* is located in the SNR 3C 58 (G130.7+03.1), probably a remnant of the historical supernova, observed starting from 1181 August 6 (Stephenson 1971; the attribution was supported by Kothes 2013). Green & Gull (1982) measured a systemic velocity

of 3C 58 about $-39\,\mathrm{km\,s^{-1}}$, which they translated to a distance of 2.6 kpc, in the Perseus spiral arm of the Milky Way. Roberts et al. (1993) measured a systemic velocity of 3C 58 about $-36\,\mathrm{km\,s^{-1}}$, which they translated to $d \sim 3.2$ kpc, using another rotation curve of the Milky Way. Having adopted this distance, Slane et al. (2004) derived a limit of $T^\infty < 1.02$ MK for BB emission from the entire surface of the pulsar. They also showed that the data were consistent with emission from NSA model for a canonical neutron star with a similar temperature.

Using an advanced approach to the kinematic distance method developed by Foster & MacWilliams (2006), Kothes (2013) derived the improved distance estimate to 3C 58, $d = 2.0 \pm 0.3$ kpc. This estimate is confirmed by the trigonometric parallax measurements of the distance to the H II region W3 (Hachisuka et al. 2006; Xu et al. 2006), which is located at $d = 2.0 \pm 0.1$ kpc a few degrees away from 3C 58 and has the same systemic velocity. A spectral modelling of pulsar wind nebula (PWN) around 3C 58 by Tanaka & Takahara (2013) is compatible with the distance of 2 kpc for assumed ages of 1 or 2.5 kyr.

We reanalysed *Chandra* data using TBABS × (NSMAXG+PL) model with fixed $d = 2$ kpc, $M = 1.4\,\mathrm{M}_\odot$ and $R = 13$ km. We obtained temperature from the entire NS surface $T^\infty = 0.57^{+0.05}_{-0.07}$ MK (for the NSMAXG model 123100). Taking the distance uncertainty into account, we obtain $L^\infty = 1.9^{+1.5}_{-1.1}\,\mathrm{erg\,s^{-1}}$.

15. *PSR J0357+3205, named Morla.* De Luca et al. (2013) put rigid bounds on the distance between 0.2 and 0.9 kpc, but the likely birthplace identified by Kirichenko et al. (2014) implies a narrower uncertainty range $d = 0.45 \pm 0.05$ kpc. The spectral analysis results in Table 2 are also quoted from Kirichenko et al. (2014), who used a neutron star atmosphere model supplemented with power law (PL; NSA+PL). For the NSA component, the best fit $k_\mathrm{B}T^\infty = 31 \pm 1$ eV has been obtained with the NSMAX model at fixed $M = 1.4\,\mathrm{M}\odot$ and $R = 13$ km. This result for T^∞ and the derived L^∞ are accepted in Table 2. The error bars embrace the result of fitting with a non-fixed radius, which gives $k_\mathrm{B}T^\infty = 36^{+9}_{-6}$ eV and $R^\infty_\mathrm{eff} = 8^{+12}_{-5}$ km at the 90 per cent confidence level. The luminosity uncertainties in Table 2 (1σ), derived from figs 2 and 3 of Kirichenko et al. (2014), also accommodate the most likely values of other fits in table 2 of Kirichenko et al. (2014).

16. *PSR J0538+2817* in the SNR Sim 147 (G180.0–01.7). The age is determined by proper motion (Kramer et al. 2003) and an analysis of the SNR (Ng et al. 2007). The quoted luminosity and temperature are mainly based on the NSA or NSA+PL spectral fits by Ng et al. (2007) ($T^\infty = 1.06 \pm 0.06$ MK, $R^\infty_\mathrm{eff} = 11.2$ km). The uncertainties in the L^∞ (but not in T^∞) in Table 2 also embrace the BB or BB+PL results ($T^\infty = 2.10 \pm 0.05$ MK, $R^\infty_\mathrm{eff} \approx 2.2$ km).

17. *CXOU J061705.3+222127* resides in the SNR IC 443. Although pulsations have not been detected, it is surrounded by a PWN. Chevalier (1999) has analysed the SNR and obtained its age. Based on the PWN properties, Swartz et al. (2015) derived constraints on the period, $P \sim 0.1$–0.6 s and the surface magnetic field $B \sim 4 \times (10^{12} - 10^{13})$ G. The fit for the canonical neutron star with a hydrogen atmosphere NSA model shows an effective temperature $k_\mathrm{B}T^\infty = 58.4^{+0.6}_{-0.4}$ eV and a bolometric luminosity $L^\infty = (2.6 \pm 0.1) \times 10^{32}\,\mathrm{erg\,s^{-1}}$ (Swartz et al. 2015; the BB fit gives $R^\infty_\mathrm{eff} \approx 1.6$ km, which is too small for radiation from the entire surface but too large for a hotspot).

18. *PSR J0633+0632*. We adopt the results of Danilenko et al. (2020). The authors argue that the pulsar is hardly associated with the previously suggested Monoceros Loop or Rosette Nebula and point out the open stellar cluster Collinder 106 as another possible birth site. For the thermal component of the spectrum, the NSMAX model of an orthogonal magnetic dipole looks most realistic among several models tried by the authors. Magnetic field strengths 1.82×10^{12} or 10^{13} G at the pole yield similar results: distance $d \sim 0.9^{+1.1}_{-0.1}$ kpc, temperature $k_\mathrm{B}T^\infty \sim 53 \pm 8$ eV, a realistic radius of an equivalent thermally emitting sphere $R^\infty_\mathrm{eff} \sim 10^{+17}_{-5}$ km, and luminosity logarithm $\log L^\infty(\mathrm{erg\ s^{-1}}) \sim 32.3 \pm 0.6$. Here, the uncertainties are at the 90 per cent confidence (in Table 2 we have reduced them to the 1σ level for the sake of uniformity). An alternative model of two hot spots using the BB+PL fit gives $k_\mathrm{B}T^\infty = 120 \pm 8$ eV, $R^\infty_\mathrm{eff} = 0.8^{+0.5}_{-0.3}$ km, $\log L^\infty = 31.4^{+0.3}_{-0.2}$, and $d = 0.8^{+0.2}_{-0.1}$ kpc.

19. *PSR J0633+1746, aka Geminga, a Musketeer.* The distance is known from measured parallax. The best spectral fit by Mori et al. (2014) with unfixed N_H consists of one BB and two PL components; the resulting thermal luminosity range covers the one obtained by De Luca et al. (2005) with fixed N_H and 2BB+PL fit, after scaling from $d = 157$ pc (an older parallax measurement, used by De Luca et al. 2005) to the updated value of $d = 250$ pc.

20. *PSR B0656+14 (J0659+1414), a Musketeer* in the SNR Monogem Ring (G201.1+08.3). The distance is known from measured parallax. The 2BB+PL fit results by Arumugasamy et al. (2018) are similar to those by De Luca et al. (2005). In Table 2, we quote the results of the G2BBPL fit of Arumugasamy et al. (2018), which is the 2BB+PL model with an added Gaussian absorption profile, which gives similar (within 20 per cent) temperatures, but more realistic effective radius of the cold component (13^{+4}_{-3} km instead of ∼20 km).

21. *PSR B0833–45 (J0835–4510)* resides in the SNR Vela (G263.9–3.3). The distance is known from measured parallax. Early estimates of the true age ranged from 5 to 50 kyr (see e.g. Stothers 1980 for references), being highly model dependent. Having analysed extended X-ray features in the SNR Vela, Aschenbach, Egger & Trümper (1995) derived $t_* = 18 \pm 9$ kyr, which agrees with the independent estimate of $t_* \sim 18$ kyr by Jenkins, Silk & Wallerstein (1976). Further analysis (Aschenbach 2002) showed that the SNR should be at least 17–23 kyr old. Therefore, we adopt the likely age interval to be 17–27 kyr, which exceeds the canonical spin-down age $t_\mathrm{c} = \mathcal{P}/(2\dot{\mathcal{P}}) = 11.3$ kyr. However, the braking index of this pulsar is smaller than the canonical value $n = 3$. Before a glitch, $n = 2.81 \pm 0.12$ (Akbal et al. 2017), which gives the corrected spin-down age (assuming negligibly small initial period) $t^*_\mathrm{c} \equiv \mathcal{P}/[(n-1)\dot{\mathcal{P}}] = 12.5 \pm 0.5$ kyr. When averaged over a large time span covering several glitches, the braking index becomes $n = 1.7 \pm 0.2$ (Espinoza, Lyne & Stappers 2017), which gives $t^*_\mathrm{c} \sim (25 - 45)$ kyr. For the luminosity, the 2BB spectral fit from table 6 of Manzali, De Luca & Caraveo (2007) yields $k_\mathrm{B}T^\infty = 93 \pm 3/186^{+5}_{-6}$ eV and $R^\infty_\mathrm{eff} = 5.06^{+0.42}_{-0.28}/0.73^{+0.09}_{-0.07}$ km for the cold/hot components at fixed $d = 287$ pc, which gives $L^\infty = 3.1^{+0.5}_{-0.4} \times 10^{32}\,\mathrm{erg\,s^{-1}}$; the hot component can also be fitted by a PL model. An NSA+PL fit at fixed $M = 1.4\,\mathrm{M}\odot$ and $R = 10$ km gives $T^\infty = 0.681 \pm 0.004$ MK and $d = 269^{+12}_{-14}$ pc, which corresponds to $L^\infty = (2.61 \pm 0.06) \times 10^{32}\,\mathrm{erg\,s^{-1}}$. Ofengeim & Zyuzin (2018) reanalysed the pulsar spectrum and obtained $T^\infty = 0.700 \pm 0.005$ MK with the NSA+PL model at fixed $d = 287$ pc, $M = 1.4\,\mathrm{M}\odot$, and $R = 13$ km. The employed NSMAX model version assumes the dipole distribution of the magnetic field over the surface and the ensuing distribution of temperature T_s (Ho, Potekhin & Chabrier 2008). In this case, the quoted T^∞ is the effective temperature derived from the total thermal luminosity, which implies $L^\infty = (4.24 \pm 0.12) \times 10^{32}\,\mathrm{erg\,s^{-1}}$. Allowing for mass and radius variations, Ofengeim & Zyuzin (2018) arrived at

the robust estimate of the effective temperature $T^\infty = 0.66^{+0.04}_{-0.01}$ MK with $M = 2.4^{+0.1}_{-1.4}\,\mathrm{M}\odot$ and $R = 10.8^{+3.7}_{-1.3}$ km.

22. *PSR B1055–52 (J1057–5226), a Musketeer.* The quoted luminosity and temperature are based on the cold component of the 2BB+PL fit by De Luca et al. (2005), which gives $T^\infty = 0.79 \pm 0.03$ MK, $R^\infty_{\rm eff} = 12.3^{+1.5}_{-0.7}$ km, $L^\infty = 4.4 \times 10^{32}\,\mathrm{erg\,s^{-1}}$ at fixed $d = 750$ pc (for the hot component, $T^\infty = 1.79 \pm 0.06$ K, $R^\infty_{\rm eff} = 0.46 \pm 0.06$ km, $L^\infty = 1.6 \times 10^{31}\,\mathrm{erg\,s^{-1}}$). Based on an analysis of optical and ultraviolet observations, Mignani, Pavlov & Kargaltsev (2010) argue that the actual distance should be smaller than the value $d = 0.73 \pm 0.15$ kpc based on the dispersion measure; they give $d \sim 200$–500 pc and scale luminosity to $d = 350$ pc. In Table 2, we show L^∞ with this scaling, including the distance uncertainty.

23. *PSR J1357–6429* in the SNR HESS J1356–645 (G309.8–02.6). The distance is evaluated by dispersion measure (Zavlin 2007). The quoted luminosity and temperature correspond to the NSA+PL fit by Chang et al. (2012). An alternative BB+PL fit gives $R^\infty_{\rm eff} \sim 2$ km, which is too small for the emission from the entire surface (Chang et al. 2012).

24. *PSR B1706–44 (J1709–4429)*, possibly in the SNR G343.1–02.3. The distance is known from measured parallax. The spectral analysis results are quoted for the best fit in McGowan et al. (2004; hydrogen NSA+PL model with fixed $R = 12$ km); uncertainties embrace other fits with the same $\chi^2_\nu = 0.84$.

25. *PSR J1740+1000.* The two distance values are given by two different electron density distribution models applied to the dispersion measure. The spectral analysis results are quoted for the 2BB fit (Kargaltsev et al. 2012). We present only results for the 2BB fit to the 'rise and fall' phase, which are based on a larger energy interval and yield plausible $R^\infty_{\rm eff} \sim 9^{+5}_{-3}$ km. The best-fitting value for the luminosity is taken from the 2BB model with fixed $k_{\rm B}T^\infty = 71$ eV. The uncertainties include phase variations, 2BB fit with non-fixed T^∞, and a contribution from the hot component.

26. *PSR J1741–2054 (Swift J174157.6–205411).* The spectral analysis results are quoted for the only acceptable BB+PL fit by Karpova et al. (2014), rescaled from $d = 1$ kpc to 0.8 kpc, which yields $R^\infty_{\rm eff} = 13.6^{+2.8}_{-2.4}$ km.

27. *PSR B1822–09 (J1825–0935).* The X-ray spectrum is well described by a 2BB model with $k_{\rm B}T^\infty = 83 \pm 4/187^{+26}_{-23}$ eV and $R^\infty_{\rm eff} = 2.04^{+0.39}_{-0.37}/0.1^{+0.05}_{-0.03}$ km, assuming a fixed distance $d = 1$ kpc (Hermsen et al. 2017). The hot component can be ascribed to the pulsed emission and the cool component to the unpulsed emission. By analogy with other pulsars, we suggest that the bolometric flux, which is mostly provided by the cool component, is powered by cooling.

28. *PSR B1823–13 (J1826–1334)* is associated with the SNR G18.0–00.7. This glitching pulsar has a low time-averaged braking index $n = 2.2 \pm 0.6$ (Espinoza et al. 2017), which gives the corrected characteristic age $t_{\rm c}^*$ in the range 24–27 kyr. The spectral analysis results listed in Table 2 are adopted from Zhu et al. (2011); they represent the BB+PL fit of Pavlov, Kargaltsev & Brisken (2008). In this case, $R^\infty_{\rm eff} = 5.1^{+0.4}_{-0.3}$ km.

29. *PSR J1836+5925* (GRO J1837+59) was discovered in 1991 as a bright γ-ray source (Lin et al. 1992). Later, it was identified as a neutron star and dubbed 'Next Geminga' (Mirabal & Halpern 2000). Its X-ray counterpart was found in the *ROSAT* data (Reimer et al. 2001) and observed with *Chandra* and *XMM–Newton* (Arumugasamy 2015). The distance estimate $d \approx 250$–750 pc is based on assumptions of γ-ray flux and beaming factor with γ-ray pulse profile modelling (Abdo et al. 2010). The BB+PL fit to the pulsar spectrum gives $k_{\rm B}T^\infty = 63.6^{+4.7}_{-6.2}$ eV and $R^\infty_{\rm eff} = 1.55^{+0.61}_{-0.25} d_{\rm kpc}$ km, whereas the fit for the canonical neutron star model, using the non-magnetic NSA+PL model, gives $k_{\rm B}T_{\rm s} = 20.7^{+6.5}_{-4.2}$ eV (in Table 2 this result is converted to the redshifted temperature and luminosity) and $d = 310^{+420}_{-170}$ pc at the 90 per cent confidence (Arumugasamy 2015).

30. *PSR B1951+32 (J1952+3252)* is associated with the SNR CTB 80 at $d \sim 2$ kpc (Strom & Stappers 2000). Proper motion of the pulsar gives $t_* = 64 \pm 18$ kyr (Migliazzo et al. 2002). The BB+PL fit to the pulsar spectrum gives $k_{\rm B}T^\infty = 130 \pm 20$ eV and $R^\infty_{\rm eff} = 2.2^{+1.4}_{-0.8}(d/2\ \mathrm{kpc})$ km, whereas the 3σ upper limit with fixed $R^\infty_{\rm eff} = 12$ km is 0.78 MK (Li, Lu & Li 2005). These values suggest $L^\infty = 1.8^{+3.0}_{-1.1} \times 10^{32}(d/2\ \mathrm{kpc})^2\,\mathrm{erg\,s^{-1}}$ and $L^\infty < 3.8 \times 10^{32}(d/2\mathrm{kpc})^2\,\mathrm{erg\,s^{-1}}$, respectively.

31. *PSR J1957+5033* has been observed in gamma rays by *Fermi*–LAT (Abdo et al. 2013) and in X-rays by *Chandra* (Marelli et al. 2015) and by *XMM–Newton* (Zyuzin et al. 2019; Zyuzin et al., in preparation). The 'pseudo-distance' of this gamma pulsar, inferred from comparison between flux and luminosity of gamma pulsars with known distance, equals 0.8 kpc (Marelli et al. 2015). The BB+PL fit yields $k_{\rm B}T^\infty = 56 \pm 7$ eV and $R^\infty_{\rm eff} = (1.5 - 7.9) d_{\rm kpc}$ km (1σ confidence). The NSA+PL fit using the model of magnetized, partially ionized hydrogen atmosphere NSMAXG with fixed $M = 1.4\,\mathrm{M}\odot$ and $R = 13$ km for the thermal component results in temperature close to the lowest value $\log T_{\rm s}(\mathrm{K}) = 5.5$ available for these models (Zyuzin et al. 2019). Zyuzin et al. (in preparation) have computed new atmosphere models, which include lower temperatures, assuming dipole magnetic fields. The polar magnetic field strengths $\sim(1$–$3) \times 10^{12}$ G are chosen to be consistent with timing for this pulsar. The atmosphere models were built for several sets of neutron star parameters. Depending on these parameters and on the inclination of the magnetic dipole axis to the line of sight, the estimates range from $k_{\rm B}T^\infty = 14 \pm 3$ eV to 21 ± 4 eV at distances $\sim$50–300 pc (Zyuzin et al., in preparation).

32. *PSR J2021+3651* powers the Dragonfly Nebula (PWN 75.2+0.1). The X-ray spectra of the pulsar and the nebula were resolved in the *Chandra* observations by Van Etten, Romani & Ng (2008). Kirichenko et al. (2015) conducted deep optical observations of this complex with the *Gran Telescopio Canarias* and reanalysed the archival *Chandra* X-ray data. They constructed the extinction–distance relation for the direction towards the pulsar and constrained the distance $d = 1.8^{+1.7}_{-1.4}$ kpc at the 90 per cent confidence. The BB+PL fit to the pulsar spectrum gives $k_{\rm B}T = 155 \pm 14$ eV and $R^\infty_{\rm eff} = 1.3^{+1.5}_{-1.0}$ km, whereas the NSA+PL fit, using the NSMAX model, gives $k_{\rm B}T = 63^{+9}_{-8}$ eV and $R^\infty_{\rm eff} = 12.0^{+19.5}_{-9.6}$ km at the 90 per cent confidence. In Table 2, we reduce the errors to the 1σ confidence level for uniformity with other data in the tables. These fits correspond to $L^\infty \sim 10^{31}$–$10^{33}\,\mathrm{erg\,s^{-1}}$, respectively. The main source of uncertainty is the poorly known distance. For fixed $R = 13$ km and $M = 1.4\,\mathrm{M}\odot$, the NSA+PL fit gives $L^\infty = 5^{+3}_{-2} \times 10^{32}\,\mathrm{erg\,s^{-1}}$.

33. *PSR B2334+61 (J2337+6151)* in the SNR G114.3+0.3. The NSA fit by McGowan et al. (2006) for the canonical neutron star model with $B = 10^{13}$ G gives $d = 1.1 \pm 0.6$ kpc and non-redshifted temperature $T_{\rm s} = 0.58^{+0.13}_{-0.25}$ MK at 90 per cent confidence, which converts into $T^\infty = 38^{+6}_{-9}$ eV and $L^\infty = (4.7 \pm 3.5) \times 10^{31}\,\mathrm{erg\,s^{-1}}$ (1σ). The authors prefer a fit with $R = 13$ km because it yields a distance compatible with $d = 3.1^{+0.2}_{-1.0}$ kpc derived from the pulsar dispersion measure using the NE2001 model of the Galactic electron distribution (Cordes & Lazio 2002, 2003). It gives the non-redshifted $T_{\rm s} = 0.65^{+0.13}_{-0.34}$ MK at 90 per cent confidence, which at the 1σ converts into $T^\infty = 46^{+6}_{-16}$ eV and $L^\infty = (1.5^{+1.0}_{-1.2} \times 10^{32}\,\mathrm{erg\,s^{-1}}$. However, the NE2001 model incorporates a void in the direction

of G114.3+0.3, likely to accommodate for the larger distance to the SNR predicted previously by Reich & Braunsfurth (1981). The modern model of the Galactic distribution of free electrons (Yao, Manchester & Wang 2017) yields the distance to the pulsar of 2.08 kpc. Moreover, Yar-Uyaniker, Uyaniker & Kothes (2004) suggested the distance to the SNR of about 700 pc from H I data analysis, which is compatible with the result of the canonical neutron star NSA fit mentioned above. We should note that the BB fit gives much higher temperature $T^\infty = 1.62 \pm 0.23$ MK and small effective radius $R^\infty_{\rm eff} \sim 0.5 d_{\rm kpc}$ km, suggesting a possible alternative interpretation of the thermal radiation as produced by hot spots.

3.3.3 *High*-B *pulsars and XINSs*

34. *PSR J0726–2612*. The reported luminosities and temperatures correspond to the best G2BB fit of Rigoselli et al. (2019a). The dispersion measure implies $d = 2.9$ kpc assuming the Galactic electron distribution, but it may be an overestimate, as discussed by Rigoselli et al. (2019a). Speagle, Kaplan & van Kerkwijk (2011) suggested that PSR J0726–2612 could be associated with the Gould belt and hence $d \lesssim 1$ kpc. The spectral fitting has been performed for fixed $d = 1$ kpc. Then the inferred effective radius for the cooler component in the G2BB fit is $R^\infty_{\rm eff} = 10.4^{+10.8}_{-2.8}$ km.

35. *PSR J1119–6127* resides in the SNR G292.2–0.5. The NSA+PL fit of the phase-averaged spectrum with fixed $R = 13$ km yields $k_{\rm B}T^\infty = 80^{+30}_{-20}$ eV and $d = 2.4^{+5.6}_{-1.8}$ kpc, while the BB+PL fit at fixed $d = 8.4$ kpc gives $k_{\rm B}T^\infty = 210 \pm 40$ eV and $R^\infty_{\rm eff} = 3^{+4}_{-1}$ km (Ng et al. 2012). Interestingly, for braking index $n = 2.684$ of this pulsar, its hosting SNR age of 4.2–7.1 kyr, evaluated at $d = 8.4$ kpc, significantly exceeds the corrected characteristic age $t_{\rm c}^* = 1.9$ kyr, which is usually considered as an upper limit to the pulsar's age (Kumar, Safi-Harb & Gonzalez 2012). We note that adopting the best-fitting distance $d = 2.4$ kpc from the spectral analysis would reduce the estimated age to 1.2–2.1 kyr, in agreement with the characteristic age. However, as follows from the analysis by Caswell, McClure-Griffiths & Cheung (2004), such a short distance should imply an unusually high interstellar absorption in the pulsar direction. It is more likely that the mean braking index may be smaller after averaging over a long time covering many glitches, which is usual for the glitching pulsars like this one (see Espinoza et al. 2017); then a lower n implies a larger $t_{\rm c}^*$.

36. *PSR B1509–58 (J1513–5908)* has a measured braking index $n = 2.832$ (Livingstone & Kaspi 2011), which gives a corrected characteristic age $t_{\rm c}^* = 1.7$ kyr. The temperature is quoted from table 4 of Hu et al. (2017). It is obtained with BB+PL fitting for fixed $d = 5.2$ kpc and $R^\infty_{\rm eff} = 13$ km. The luminosity in our Table 2 corresponds to these data. However, $R^\infty_{\rm eff}$ is poorly constrained by the observations, and fig. 10 of Hu et al. (2017) shows a larger luminosity interval, $1.0 \times 10^{33} - 1.5 \times 10^{34}$ erg s^{-1}.

37. *PSR J1718–3718*. The luminosity and temperature estimates are quoted from Zhu et al. (2011). The BB model preferred by the authors leads to $k_{\rm B}T^\infty = 186^{+19}_{-18}$ eV, $R^\infty_{\rm eff} = 1.8^{+1.7}_{-0.6}(d/4.5\ {\rm kpc})$ km and $L^\infty = 4^{+5}_{-2} \times 10^{32} (d/4.5\ {\rm kpc})^2$ erg s^{-1}. On the other hand, the NSA model with the canonical neutron star parameters, assuming $d = 4.5$–10 kpc, leads to $k_{\rm B}T_{\rm s} = 75$–97 eV, which gives $k_{\rm B}T^\infty = 57$–74 eV and $L^\infty = (2.4$–$6.7) \times 10^{32}$ erg s^{-1}.

38. *PSR J1819–1458* is the only 'rapid radio transient' registered in X-rays (see Gençali & Ertan 2018 and references therein). The 2GBB fit by Miller et al. (2013) (the only one with $\chi^2_\nu < 1.1$ at $d = 3.6$ kpc) gives $k_{\rm B}T^\infty = 138.2 \pm 0.9$ eV and $R^\infty_{\rm eff} = 8^{+5}_{-4}$ km. The inferred value of L^∞ in our Table 2 is consistent with the unabsorbed bolometric flux for this model. The errors accommodate those alternative spectral fits (BB and GBB) in table 2 of Miller et al. (2013) that have plausible $R^\infty_{\rm eff} < 20$ km.

39. *RX J0420.0–5022*. The reported results are based on the best fit by Haberl et al. (2004; GBB model for the canonical neutron star) and the results listed by Kaplan & van Kerkwijk (2009).

40. *RX J0720.4–3125*. The spin period of this object is the longest among all currently known XINSs (Hambaryan et al. 2017; the period was previously thought to be twice shorter because of comparable pulses from two antipodal spots). This XINS shows significant variability of its X-ray spectrum (Hohle et al. 2012a, b). Its distance is known from measured parallax. An analysis of *Chandra* co-added spectra with the GBB model (Hohle et al. 2012a) yields L^∞ and T^∞ quoted in Table 2 with $R^\infty_{\rm eff} = 4.5^{+1.3}_{-1.1}$ km at $d = 0.3$ kpc. Hambaryan et al. (2017) performed a phase-resolved spectral analysis with more physical models of condensed surface and magnetized atmosphere, taking a non-uniform temperature distribution into account. They found phase-dependent best-fitting temperature values at magnetic poles in the range $k_{\rm B}T^\infty \approx 98$–115 eV,

41. *RX J0806.4–4123*. The BB and GBB fits by Haberl et al. (2004) give $k_{\rm B}T^\infty = 104 \pm 4$ eV and 92 ± 4 eV, respectively. The luminosities are derived assuming $R^\infty_{\rm eff} = 1.3$ km as given by Kaplan & van Kerkwijk (2009) for the latter fit. They agree with the luminosities in Viganò et al. (2013).

42. *RX J1308.6+2127 (RBS1223)*. The distance $d \sim 380$ pc has been obtained from the spectral analysis together with the temperature and luminosity by Hambaryan et al. (2011). Of three different age estimates suggested by Motch et al. (2009), only the one quoted in Table 2 is compatible with this distance. For $d = 380$ pc, the spectral fit implies a large non-redshifted radius $R = 16 \pm 1$ km, which may suggest that the actual distance is closer to the estimate by Motch et al. (2009) for the possible neutron-star birthplace, $d = 260 \pm 50$ pc. Alternatively, this may imply a higher mass, which would yield a large $R^\infty_{\rm eff}$. The effective temperature for this radius is 7×10^5 K in the local reference frame. The corresponding luminosity at infinity is $L^\infty = (3.3 \pm 0.5) \times 10^{32}$ erg s^{-1}. The model temperature distribution over the surface has maximum at $k_{\rm B}T_{\rm s} = 105^{+2}_{-4}$ eV (the minimum is much lower). An alternative BB fit for the canonical neutron star model gives $k_{\rm B}T_{\rm s} = 100$ eV and dilution factor 0.34, which corresponds to $L^\infty \sim 2.6 \times 10^{32}$ erg s^{-1}.

43. *RX J1605.3+3249 (RBS1556)*. The age estimate is based on table 4 of Tetzlaff et al. (2012). Posselt et al. (2007), using different models of the hydrogen column density, derived distances of 390 and 325 pc. On the other hand, Motch et al. (2005) link the source with the Sco OB2 association within the Gould Belt, at a mean distance of 120–140 pc. Tetzlaff et al. (2012) argue that the neutron star was probably born in the Octans association from a supernova at $d = 140^{+6}_{-19}$ pc. They adopt the current distance of 300–400 pc from Posselt et al. (2007), which requires rather large (though not impossible) space velocity ∼550 km s^{-1}. Pires et al. (2019) have performed a timing and spectral analysis of *XMM–Newton* observations. The best multi-epoch fit G2BB at fixed $d = 300$ pc for the cooler component gives $k_{\rm B}T^\infty = 60.9^{+1.7}_{-1.5}$ eV and $R^\infty_{\rm eff} = 16.2^{+0.6}_{-1.1}$ km, in which case $L^\infty = (4.7 \pm 0.5) \times 10^{32}$ erg s^{-1} (which we adopt as an upper bound); the hotter component with $k_{\rm B}T^\infty \approx 117$ eV and $R^\infty_{\rm eff} \approx 1.34$ km adds about 10 per cent to the total energy flux. Multi-epoch fits by different NSA models, modified by a broad Gaussian absorption line at energy 385 ± 10 eV, give $d \sim 110$–130 pc and $\log T_{\rm s}({\rm K}) \approx 5.6$–5.8, corresponding to $\log L^\infty({\rm erg\ s^{-1}}) \sim 31.4 \pm 0.6$ (providing the lower bounds in Table 2). Note that Pires et al. (2019) have disproved a previously reported spin

periodicity of this X-ray source. Malacaria et al. (2019) performed a joint analysis of the *NICER* and *XMM–Newton* data. These authors found that $d \sim 350$ pc is hard to accommodate with their data, while a possible distance ∼100–200 pc is consistent with the data. The G2BB model gives $T^\infty = 63^{+7}_{-6}/119^{+6}_{-4}$ eV and $L^\infty \sim$ (3–5) $\times 10^{32}$ erg s^{-1}. Atmosphere models NSA and NSMAXG, modified by an absorption line at ∼450 eV, yield similar effective temperatures $k_{\rm B}T_{\rm s} = 47.0 \pm 0.5$ eV (for fixed $M = 1.4\,{\rm M}\odot$ and $R = 10$ km, which requires $d = 92 \pm 5$ pc) and $k_{\rm B}T_{\rm s} = 46.2^{+1.7}_{-2.3}$ eV (at fixed $d = 100$ pc, which gives $M = 2.04^{+0.19}_{-0.49}{\rm M}\odot$, $R = 15.6^{+0.6}_{-0.8}$ km; all errors are at 90 per cent confidence). These results lead to $L^\infty = (3.7 \pm 0.2) \times 10^{31}$ erg s^{-1} (NSA) or $L^\infty = (8.8 \pm 1.0) \times 10^{31}$ erg s^{-1} (NSMAXG), within the bounds provided by the analysis of Pires et al. (2019).

44. *RX J1856.5–3754*, aka the Walter star, is the first discovered neutron star with purely thermal spectrum (Walter, Wolk & Neuhäuser 1996). Its likely birthplace is the Upper Scorpius OB association, which gives $t_* = 420 \pm 80$ kyr (Mignani et al. 2013). The distance is known from parallax measurements. The spectral analysis performed by Ho et al. (2007) with the model of a thin partially ionized hydrogen atmosphere with magnetic field $B \sim$ (3–4) $\times 10^{12}$ G, being scaled to the updated distance $d = 123^{+11}_{-15}$ pc (Walter et al. 2010), leads to $k_{\rm B}T^\infty = 37.4 \pm 0.3$ eV, $R = 12.1^{1.3}_{-1.6}$ km, $M = 1.48^{+0.16}_{-0.19}\,{\rm M}\odot$ and $L^\infty = 5.8 \pm 0.2$ erg s^{-1} (Potekhin 2014). Alternative 2BB, 2BB+PL, and 3BB fitting models have been presented by Sartore et al. (2012) and Yoneyama et al. (2017). They yield $k_{\rm B}T^\infty = 39^{+5}_{-3}/62.4^{+0.6}_{-0.4}$ eV and $R^\infty_{\rm eff} \sim 12/4.7$ km for two BB components, which give similar luminosities at infinity, $\sim 4 \times 10^{31}$ erg s^{-1} each.

45. *RX J2143.0+0654 (RBS1774, 1RXS J214303.7+065419).* The quoted luminosities and temperatures are based on the spectral analysis by Schwope et al. (2009), who supplemented the joint *Chandra* and *XMM–Newton* observations with deep optical observations. The lower luminosity bound $L^\infty = 6.3 \times 10^{31}$ erg s^{-1} corresponds to the colder component ($k_{\rm B}T^\infty = 40$ eV, $R^\infty_{\rm eff} = 13.8$ km) at the lowest possible distance $d = 250$ pc. The hot circular spot with radius of 1.6 km and $k_{\rm B}T^\infty = 104$ eV adds approximately 10^{31} erg s^{-1}, which should be doubled for two antipodal hot spots. The colder component rescaled to fiducial distance $d = 410$ pc corresponds to $L^\infty \approx 1.7 \times 10^{32}$ erg s^{-1}, which is adopted as the upper limit in Table 2. By order of magnitude, these estimates agree with Zampieri et al. (2001), who found $L^\infty \sim 10^{32}\,(d/300\,{\rm pc})^2$ erg s^{-1} On the other hand, if the optical flux measured by Schwope et al. (2009) has a non-thermal origin, then one can rely on the analysis of this source by Cropper et al. (2007), based on BB or GBB models. At fixed $d =$ 300 pc it gives $k_{\rm B}T^\infty \approx$ 101–104 eV, $R^\infty_{\rm eff} \approx 2$ km, and $L^\infty \sim$ (5–6) $\times 10^{31}$ erg s^{-1} (we adopt it as a lower bound). Alternative fits for the canonical neutron star model and magnetized NSA give smaller temperatures $k_{\rm B}T^\infty \sim$ 24–40 eV and luminosities $L^\infty \approx$ (0.7–6) $\times 10^{31}$ erg s^{-1}, but show a poor statistical significance $\chi^2_\nu \sim 2$ (Cropper et al. 2007).

3.3.4 *Upper limits on cooling-powered thermal emission*

46. *PSR J0007+7303* is a radio-quiet pulsar associated with the SNR CTA 1 (G119.5+10.2). It was observed in X-rays with *Chandra*, *XMM–Newton*, and *Suzaku* (Halpern et al. 2004; Caraveo et al. 2010; Lin et al. 2010, 2012) and in γ-rays with *Fermi*–LAT (Abdo et al. 2012). The distance of 1.4 ± 0.3 kpc is estimated from the velocity of an H I shell associated with the SNR CTA 1 (Pineault et al. 1993). The age of 9.2 kyr is derived from modelling the dynamics and spectra of the PWN and the SNR CTA 1 using estimates of the molecular mass in the vicinity of the complex (Martín, Torres & Pedaletti 2016). The analysis of the pulsar X-ray spectrum has been performed by Caraveo et al. (2010). The BB+PL fit gives $k_{\rm B}T^\infty = 102^{+32}_{-18}$ eV, $R^\infty_{\rm eff} = 0.64^{+0.88}_{-0.20}d_{1.4}$ km and thermal luminosity $L^\infty = (3.6 \pm 1.4) \times 10^{30} d^2_{1.4}$ erg s^{-1}, where $d_{1.4} = d/(1.4{\rm kpc})$. The NSA+PL fit gives $k_{\rm B}T^\infty = 54^{+25}_{-16}$ eV, $R^\infty_{\rm eff} = 4.9^{+1.8}_{-4.7}d_{1.4}$ km, and $L^\infty = 3.9^{+2.6}_{-1.3} \times 10^{30} d^2_{1.4}$ erg s^{-1}. A PL without a thermal component also provides a good fit ($\chi^2_\nu = 0.74$) therefore the above estimates of thermal luminosity can only provide an upper limit.

47. *PSR B0531+21* is located in the Crab Nebula, a remnant of the historical supernova, observed starting from 1054 July 4 (e.g. Stephenson & Green 2003). Trimble (1973) estimated a range of distances between 1.4 and 2.7 kpc based on a variety of lines of evidence. The L^∞ and T^∞ limits in Table 2 are determined from fig. 5 of Weisskopf et al. (2011) at the 3σ confidence level, assuming $M = 1.4\,{\rm M}\odot$, $R = 12$ km, and $d = 2$ kpc.

48. *PSR B1727–47 (J1731–4744)* is located in the SNR RCW 114 (G343.0–06.0). Shternin et al. (2019) measured the proper motion of the pulsar and determined its likely birthplace, distance, and age. The spectral analysis has been performed by Zyuzin, Karpova & Shibanov (in preparation) using the NSMAXG+PL model with fixed $d = 0.75$ kpc and $R = 12.5$ km.

49. *PSR J2043+2740* is located near the edge of the Cygnus Loop (SNR G074.0-08.6), whose age is ∼10–20 kyr at distance 735 ± 25 pc (Fesen et al. 2018). However, the association with this SNR is very uncertain. Therefore, the distance based on the dispersion measure is usually adopted: $d = 1.8$ kpc in early works (Becker et al. 2004; Zavlin & Pavlov 2004; Zavlin 2009) or $d =$ 1.48 kpc in more recent papers (Testa et al. 2018). This pulsar has also been observed in gamma rays (Abdo et al. 2013) and in optical bands (Beronya et al. 2015; Testa et al. 2018); its multiwavelength optical-to-gamma spectrum has been discussed by Testa et al. (2018). There was only one 12-ks observation of this pulsar in X-rays by *XMM–Newton* in 2002, which gathered about one hundred counts. Zavlin & Pavlov (2004) and Zavlin (2009) argued that this emission should be mostly thermal, since a PL fit gave implausibly large photon index ∼5. For a fixed $d = 1.8$ kpc, these authors obtained effective temperatures ranging from 0.5 to 0.9 MK and emitting radii from ∼9 down to ∼2 km, with $L^\infty \sim$ (2–4) $\times 10^{31}$ erg s^{-1}, depending on a fit model. For a hotspot with radius 0.47 km, inferred from the magnetic dipole model (e.g. Manchester & Taylor 1977), they obtained $L^\infty \sim 10^{30}$ erg s^{-1}. However, this last estimate would imply an implausibly small distance $d \lesssim 0.4$ kpc. On the other hand, an analysis of the same data by Becker et al. (2004) showed a poor statistics for the BB or 2BB fits, but gave an acceptable PL fit with power index of $3.1^{+1.1}_{-0.6}$. Because of all these uncertainties, we treat the maximum temperature and luminosity estimates derived by Zavlin & Pavlov (2004) as upper limits. A longer observation of this object would be desirable to shed light on the origin of its X-ray emission.

50. *PSR B2224+65 (J2225+6535)* is associated with the Guitar bow-shock Hα nebula. Its radio parallax is $1.20^{+0.17}_{-0.20}$ mas (Deller et al. 2019). Only non-thermal X-ray flux has been registered from this pulsar. Hui & Becker (2007) estimated its X-ray luminosity as $L_X \sim (1-2)\,d^2_{\rm kpc} \times 10^{30}$ erg s^{-1}. It was not clear, whether the bulk of these observed X-rays originated from the pulsar magnetosphere or from the PWN (Hui et al. 2012). The analysed data only include photon energies above 0.7 keV, which leaves a bolometric correction very uncertain. Hui & Becker (2007) also estimated the upper bound on the temperature of a hotspot $T^\infty < 1.3$ MK by adding a BB component to the best-fitting PL model and assuming a polar cap of radius 175 m, derived from the standard dipole model (e.g. Manch-

ester & Taylor 1977). We adopt this constraint as a conservative upper limit to the temperature. A more restrictive estimate $T^\infty < 0.61$ MK (3σ) was derived by Hui & Becker (2007) assuming that the thermal flux is emitted from the whole surface of a canonical neutron star. It corresponds to bolometric flux $L^\infty < 1.7 \times 10^{32}$ erg s^{-1}, which we take as a conservative upper limit to the thermal luminosity.

3.3.5 Hot spots on the surfaces of old rotation-powered pulsars

51. *PSR B0114+58 (J0117+5914).* The distance $d = 1.77 \pm 0.53$ kpc has been inferred from the dispersion measure by Rigoselli & Mereghetti (2018). The authors obtained the quoted T^∞ and L^∞ by an analysis of archival *XMM–Newton* observations with the BB model. They estimated the effective radius of a plane hotspot on the stellar surface to be 450^{+110}_{-90} m; in Table 2 we list half of this number for the radius of an equivalent sphere $R^\infty_{\rm eff}$.

52. *PSR B0943+10 (J0946+0951).* We mainly rely on the spectral analysis by Rigoselli et al. (2019b). Namely, we have selected a fit model of the partially ionized hydrogen atmosphere with $B \approx 2 \times 10^{12}$ G in the so-called B-mode, where the X-ray flux has minimum. This fit yields $k_{\rm B}T^\infty = 82^{+3}_{-9}$ eV and $R^\infty_{\rm eff} = 170^{+45}_{-25}$ m. The condensed surface models give $k_{\rm B}T^\infty \sim$ 200–220 eV and $R^\infty_{\rm eff} \sim 40 - 60$ m. The thermal component of the BB+PL fit yields $k_{\rm B}T^\infty = 210 \pm 20$ eV and $R^\infty_{\rm eff} = 41^{+10}_{-9}$ m. The corresponding luminosity range is shown in Table 2; it agrees with the range of the unabsorbed X-ray flux given in that reference.

53. *PSR B1133+16 (J1136+1551).* The distance is known from measured parallax. Over 2/3 of this pulsar's luminosity in the 0.3–2 keV range is non-thermal; the radius of equivalent emitting sphere is $R^\infty_{\rm eff} = 17^{+7}_{-5}$ m (Szary et al. 2017). The redshifted luminosity and temperature in Table 2 are derived from the non-redshifted values in table 6 of that paper.

54. *PSR J1154–6250.* The listed distances correspond to two models of the Galactic electron density distribution; the pulsar's projection on the Cru OB1 association is most likely a chance coincidence (Igoshev et al. 2018). The quoted bolometric luminosity is obtained from the unabsorbed flux $(7.5 \pm 2.2) \times 10^{-15}$ erg cm^{-2} s^{-1} at $d = 1.36$ kpc (table 3 of the cited reference). It assumes thermal interpretation. However, it may turn out to be only an upper limit, since the PL model fits the spectrum equally well (Igoshev et al. 2018).

55. *PSR B1929+10 (J1932+1059).* The distance is known from measured parallax. The quoted thermal luminosity from Misanovic, Pavlov & Garmire (2008) is scaled to the updated distance $d = 310$ pc (Verbiest et al. 2012) from $d = 361$ pc adopted by the authors; the scaled radius of an equivalent emitting sphere $R^\infty_{\rm eff} = 28^{+5}_{-4}$ m is obtained for the BB+PL spectral model. It may turn out to be only an upper limit, since the PL model yields an acceptable fit with only slightly larger χ^2_ν.

3.4 Excluded objects

Here we do not consider the soft gamma repeaters and anomalous X-ray pulsars (SGR/AXPs), luminous neutron stars which reveal powerful bursts. Probably they are magnetars, neutron stars with superstrong magnetic fields $B \sim 10^{14} - 10^{16}$ G, which power their bursting activity (see e.g. Mereghetti, Pons & Melatos 2015; Kaspi & Beloborodov 2017, for recent reviews). Their persistent radiation, albeit thermal-like in the soft X-ray band, can hardly be related to passive cooling (see Viganò et al. 2013; Potekhin & Chabrier 2018). It is thought to arise from a complicated blending of surface thermal emission distorted by the presence of a highly magnetized atmosphere, then Comptonized by currents in the magnetosphere, which can further result in surface heating via return currents (e.g. Kaspi & Beloborodov 2017, and references therein). The surface may also be heated by energy release in the crust, driven, for example, by magneto-thermal (e.g. Viganò et al. 2013) or magneto-thermoplastic evolution (Li, Levin & Beloborodov 2016).

As mentioned in Section 3.1, the millisecond pulsars cannot be used for direct testing the cooling theory. They have been recycled during accretion from a binary companion (e.g. Bisnovatyi-Kogan 2006 and references therein), and their ages (typically of the order of gigayears) greatly exceed the passive cooling timescale. Therefore, thermal radiation registered from the millisecond pulsars originates from late-stage heating, either the heating of hot spots by fast particles from the magnetosphere or the internal heating due to slow non-equilibrium processes (Gonzalez & Reisenegger 2010 and references therein). The heating hypothesis was supported by the detection of the far-UV part of the thermal emission from the bulk of the surface of the closest ($d = 156.3$ pc) millisecond pulsar J0437–4715 (Kargaltsev, Pavlov & Romani 2004; Durant et al. 2012) with $t_{\rm c} = 6.64$ Gyr and possibly also from the surface of the millisecond pulsar J2124–3358 (Rangelov et al. 2017) with Lutz–Kelker-bias-corrected distance $d = 300^{+70}_{-50}$ pc (Verbiest et al. 2012) and proper-motion-corrected $t_{\rm c} = 10.7$ Gyr (Manchester et al. 2005). Recently, modelling the cool thermal component of the UV–X-ray spectrum of PSR J0437–4715 has resulted in the estimates $R = 13^{+0.9}_{-0.8}$ km and $T^\infty = (2.3 \pm 0.1) \times 10^5$ K, which correspond to $L^\infty = (5.3 \pm 1.0) \times 10^{30}$ erg s^{-1} (González-Caniulef, Guillot & Reisenegger 2019). Upper limits to thermal fluxes from some millisecond pulsars can be found in González-Jiménez et al. (2015). A recent study of the millisecond pulsar J0952–0607 (Ho, Heinke & Chugunov 2019) provides an upper bound on its luminosity $L^\infty \lesssim 10^{31}$ erg s^{-1}. Thermal emission has also been identified from hot ($kT^\infty = 260^{+30}_{-20}$ eV) polar cap of the very old ($t_{\rm c} = 16.5$ Gyr) millisecond pulsar J1909–3744 with well known mass and distance, which gives $L^\infty \approx 1.5 \times 10^{30}$ erg s^{-1} (Webb et al. 2019).

We have discarded PSR B0355+54, PSR B1916+14, and PSR J1734-3333 from the catalogue of Zhu et al. (2011) because their effective temperatures and thermal luminosities (probably of hot spots, as suggested by small effective radii) appear to be poorly constrained. We have also discarded PSR B0950+08 and PSR B0823+26 from the same catalogue. In the case of PSR B0823+26, recent observations and analysis (Hermsen et al. 2018) reveal a small effective emitting area ($R^\infty_{\rm eff} < 100$ m) for a thermal-like component of the spectrum; moreover, this component is only observed in the 'bright mode' of the pulsar (in the 'null mode' the X-ray flux is below detection threshold), which excludes its interpretation in terms of passive cooling. In the case of PSR B0950+08, its effective surface temperature $\sim$(1–3) $\times 10^5$ K and bolometric thermal luminosity $L^\infty = 8^{+7}_{-4} \times 10^{29}$ erg s^{-1}, obtained recently by Pavlov et al. (2017), should be caused by reheating at its characteristic age $t_{\rm c} = 17.5$ Myr (as for the above-mentioned millisecond pulsars), whereas treating $t_{\rm c}$ as only an upper limit to the true age makes this constraint too loose to be useful.

Recently, Guillot et al. (2019) have obtained an upper bound $T_{\rm s} < 4.2 \times 10^4$ K for slowly rotating ($\mathcal{P} = 8.51$ s) old (proper-motion-corrected $t_{\rm c} = 333$ Myr) PSR J2144–3933, which makes it the coldest known neutron star and indicates that the integrated power of reheating processes in slowly rotating neutron stars may be below

10^{28} erg s^{-1}. We have not included this result in the table because it does not constrain the theory of passive cooling.

The neutron star candidate 1WGA J1952.2+2925 in PWN DA 495 near the centre of SNR G065.7+01.2 has a pure thermal spectrum (Karpova et al. 2015), but its age, distance, and temperature are very uncertain. Pulsars J0554+3107 and J1105-6037 show thermal emission in the X-ray spectra (Zyuzin, Karpova & Shibanov 2018), but due to small count statistics it is hard to estimate their thermal luminosities. The X-ray source RX J0002.9+6246, which was listed in several cooling neutron star collections starting from Page et al. (2004), turned out to be an ordinary star (Esposito et al. 2008).

4 THEORY VERSUS OBSERVATIONS

Let us compare the cooling theory of INSs with the observational data described in Section 3. We will demonstrate the effects of heat blanketing envelopes, stellar mass, and models of nucleon superfluidity on the cooling curves. All these effects have been described in the literature. Our aim is to attract attention to some modern theoretical models and use the updated set of observational data.

To simulate neutron-star cooling, we use the numerical code described in Potekhin & Chabrier (2018). The physics input is mainly as reviewed in Potekhin et al. (2015), supplemented by recent updates of the superfluid pairing gaps (Ding et al. 2016) and the modified Urca reaction rates (Shternin, Baldo & Haensel 2018). The EoS and the proton fraction in the core correspond to the BSk24 model (Pearson et al. 2018).

4.1 Effects of heat blanket for a star of fixed mass

Let us first check the effects of heat blanketing envelopes (Section 2.2) against a restricted data set of cooling INSs with estimated ages. Fig. 1 shows cooling curves for a non-superfluid neutron star of mass $M = 1.4\,\mathrm{M}\odot$. The direct Urca processes are forbidden in such a star (for the BSk24 model of matter composition that we use), so that its neutrino cooling is mostly powered by the modified Urca processes. From a practical point of view, it makes sense not to consider fast cooling without superfluidity because this would produce luminosities substantially below all observations. The dashed curve in the figure shows the cooling of a neutron star with ground-state crust, where the blanketing envelope consists of iron up to $\rho \approx 8 \times 10^6\,\mathrm{g\,cm^{-3}}$ and of nickel isotopes at deeper layers. The solid curve shows the case where the ground-state crust is replaced by carbon and then by oxygen up to the densities and temperatures of carbon and oxygen fusion, respectively (Potekhin & Chabrier 2012). The dot–dashed curve corresponds to the case where the ground-state matter is replaced by helium at $\rho < 10^9\,\mathrm{g\,cm^{-3}}$. The shaded strips are formed by cooling curves calculated assuming different possible amount of accreted material.

Points and error bars in Fig. 1 show redshifted luminosities L^∞ versus ages t_*. Error bars give uncertainties (1σ) of the measured values, and downward arrows mark 3σ upper limits on L^∞.

According to Fig. 1, variations of chemical composition in the heat blanket of a $1.4\,\mathrm{M}_\odot$ star allow one to explain much more objects, than in case of one star with fixed heat blanket, but not all selected objects. The coldest stars at the neutrino cooling stage have thermal luminosities far below the theoretical curves (we will see in Section 4.2 that this can be explained by enhanced neutrino emission for INSs with large masses).

In contrast, the evolution of INSs at the photon cooling stage is not regulated directly by their neutrino emission. However, INSs

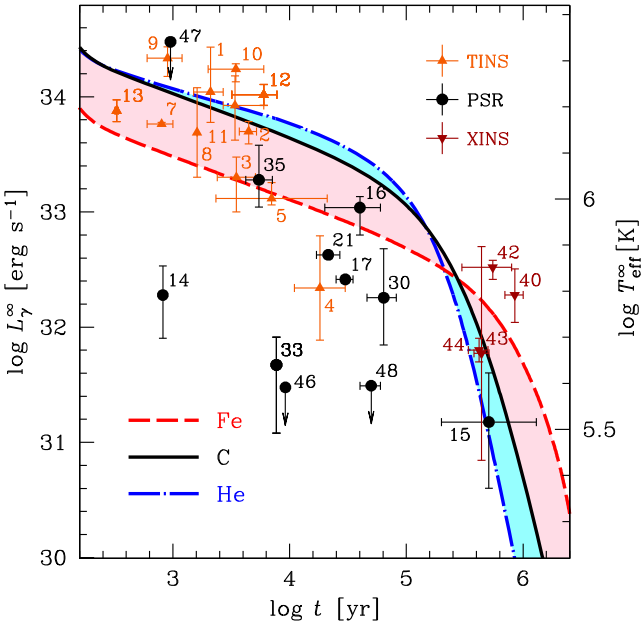

Figure 1. Cooling curves of neutron stars with $M = 1.4\,\mathrm{M}\odot$, $R = 12.6\,\mathrm{km}$ and different heat blanketing envelopes: purely ground-state (the dashed curve) and replaced with carbon (the solid curve) or helium (the dot–dashed curve). The left vertical axis is the thermal photon luminosity, the right axis is the effective temperature, as seen by a distant observer. The curves are compared with the data on INSs with estimated ages and luminosities from Table 2. The data are plotted as indicated in the legend (colour online), for different neutron star classes: thermally emitting INSs (TINSs, including CCOs), pulsars (PSRs, including high-B pulsars), and XINSs. The error bars show uncertainties (typically 1σ) and the arrows correspond to upper limits (at 3σ confidence).

observed at the photon cooling stage could not be very powerful neutrino emitters at the previous stage. Otherwise, they would have lost too much heat and would now be too faint to be observed. As seen from Fig. 1, these non-superfluid INSs are reasonably compatible with the standard neutrino cooling provided by the modified Urca processes.

4.2 Effects of fast cooling processes and superfluidity

The proton fraction in the neutron star core grows with ρ. In central regions of the stars with $M > M_{\rm DU} \sim 1.6\,\mathrm{M}\odot$ (in the BSk24 model), the proton fraction is above the threshold for opening the powerful neutrino emission via direct Urca processes (see Section 2.4). The higher M above this threshold, the larger the central part of the core where the direct Urca processes operate.

In Fig. 2 we compare theoretical luminosities and surface temperatures of neutron stars of different masses with all data in Table 2 (not only the objects with known t_*). When available, we keep using t_* for the age estimate. Otherwise we use characteristic ages and treat them as upper limits (which are, however, not strict, as discussed in Section 3.2). If the observed thermal luminosity is thought to be produced by hot spots, the thermal flux from the interior must be smaller, and we supplement error bars by dotted arrows directed downward.

According to the theory, neutron star cooling can be greatly affected by nucleon superfluidity (see Section 2.4). In Fig. 2, we show cooling curves of superfluid neutron stars of different masses.

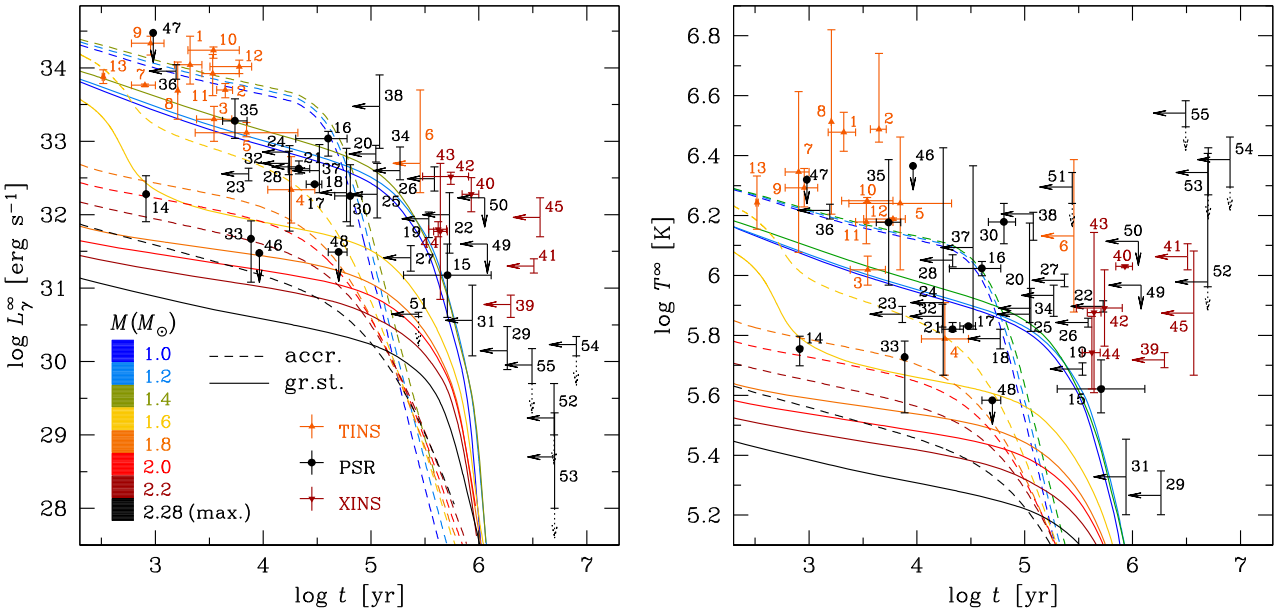

Figure 2. *Left-hand panel*: Luminosities L_γ^∞ plotted against ages t from Table 2 compared with theoretical cooling curves for INSs with different masses (coded with colour), non-accreted (the solid curves) and accreted (the dashed curves) blanketing envelopes, and with the superfluidity model MSH+BS+TTav. The data for different INS classes (TINSs, PSRs, XINSs) are plotted with the same symbols and colors as in Fig. 1. The error bars show uncertainties and the arrows show upper limits. If the detected thermal radiation is thought to originate entirely from hot spots, the vertical error bars are supplemented by the broken downward arrows (meaning that the non-detected thermal component can be fainter). The horizontal error bars show the estimated age intervals, whenever available; otherwise horizontal arrows mark less reliable characteristic ages. *Right-hand panel*: the same for temperatures $T_{\rm eff}^\infty$ instead of luminosities. See text for details.

The stars are supposed to have either non-accreted (ground state) heat blanketing envelopes or accreted envelopes composed of helium and carbon. The critical temperatures for singlet neutron, singlet proton, and triplet neutron types of pairing as functions of density are evaluated using the MSH, BS, and TTav parametrizations of Ho et al. (2015). They are based on theoretical models computed, respectively, by Margueron et al. (2008), Baldo & Schulze (2007), and Takatsuka & Tamagaki (2004). For each given type of the blanketing envelope, the cooling curves are close to one another as long as $M < M_{\rm DU}$, but they become drastically different at higher M.

Comparing the right-hand and left-hand panels of Fig. 2, we see that if, instead of L^∞, we employ observed surface temperatures T^∞ neglecting information on effective emitting sphere radius $R_{\rm eff}^\infty$, then the agreement between the theory and the data becomes generally worse and some upper limits become useless. This illustrates the importance of luminosity estimates for the cooling theory (as was previously stressed, e.g. by Viganò et al. 2013; also see the discussion in Section 3.1).

Comparing the data with the computed curves, we see that the models with iron blanketing envelopes are unable to explain the hottest of the younger stars. Accreted envelopes improve the agreement, as we have already seen in Section 4.1 for the particular case of $M = 1.4\,{\rm M}\odot$ star. The enhanced neutrino cooling through the direct Urca process for the more massive stars allows us to explain low thermal luminosities of some sources at the neutrino cooling stage, which remained unexplained in Fig. 1.

The superfluid stars cool down faster at the photon cooling stage, compared with their non-superfluid counterparts discussed in Section 4.1. The faster cooling is explained by the heat capacity $C(\widetilde{T})$ reduced by superfluidity (see Section 2.4). As a consequence, according to Fig. 2, some XINSs are significantly hotter than they should have been at their estimated ages. One explanation may be that some reheating is operating in these objects, but another possibility is an overestimation of the critical temperature of neutrons in our cooling models.

Recent studies have demonstrated that the effects of many-body correlations on baryon superfluidity may strongly reduce the superfluid gap for the triplet type of pairing (e.g. Ding et al. 2016 and references therein; see Sedrakian & Clark 2019 for a discussion). To test an effect of such gap reduction on neutron star cooling, we multiply the TTav gap, used in Fig. 2, by an appropriate suppression factor. We evaluate this factor as the ratio of the neutron triplet pairing gaps calculated with and without inclusion of the many-body correlations (Ding et al. 2016). In this example, we rely on the results obtained with the Av18 effective potential that underlies the TTav gap model. Although the TTav critical temperature $T_{\rm cn}$, as parametrized by Ho et al. (2015), has a maximum of 5.5×10^8 K at $\rho \approx 4 \times 10^{14}\,{\rm g\,cm^{-3}}$, the reduced $T_{\rm cn}$ barely reaches 10^8 K at $\rho \approx 3 \times 10^{14}\,{\rm g\,cm^{-3}}$ and falls below 10^7 K at $\rho \gtrsim 6 \times 10^{14}\,{\rm g\,cm^{-3}}$. The resulting cooling curves are shown in Fig. 3. The smaller pairing gap cannot strongly reduce the heat capacity of neutrons in the star cores. Moreover, the neutrons remain normal (non-superfluid) in a substantial range of densities in the core. The heat capacity remains relatively large, and the temperature decreases slower. Thus, our calculations demonstrate that thermal luminosities of rather warm and old cooling INSs strongly depend on the neutron superfluidity in their cores. The agreement with observations of relatively old cooling neutron stars improves substantially by reduction of the neutron triplet pairing gap. This confirms the analogous conclusions, recently obtained by other authors based on a smaller sample of cooling neutron stars (Taranto, Burgio & Schulze 2016; Fortin et al.

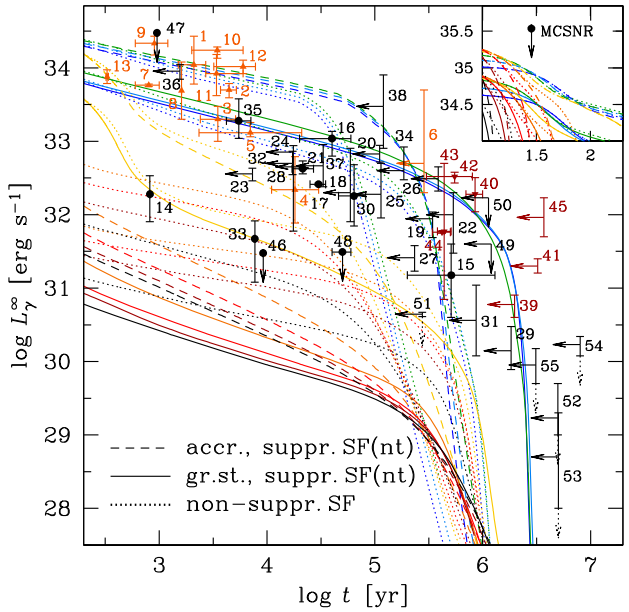

Figure 3. The same as in Fig. 2, but with suppressed triplet superfluid gap. The cooling curves with non-suppressed gap from Fig. 2 are reproduced by the dotted lines for comparison. The inset shows the early cooling compared with the tentative upper limit to the luminosity of a compact object in MCSNR J0535–6916 (the remnant of SN 1987A) according to Cigan et al. (2019).

2018; Beznogov et al. 2018; Wei, Burgio & Schulze 2019; Wei et al. 2020), and also by analysis of thermal luminosities of soft X-ray transients in quiescence (Fortin et al. 2018; Potekhin, Chugunov & Chabrier 2019).

The inset of Fig. 3 shows early cooling ($10\,\mathrm{yr} < t < 200\,\mathrm{yr}$ and $L^\infty > 10^{34}\,\mathrm{erg\,s^{-1}}$) compared with a tentative upper limit to the luminosity of a possible compact object in the SNR MCSNR J0535–6916, left after the SN 1987A explosion. This limit, $L^\infty < 90\,L_\odot$ at $t = 28.5\,\mathrm{yr}$, was obtained by Cigan et al. (2019) by an analysis of high-resolution ALMA images of dust and molecules in the SN 1987A ejecta; implications of this possible detection for the neutron star cooling theory were discussed by Page et al. (2020).

Our analysis is illustrative and naturally incomplete. For instance, we have used one model EoS. Other EoSs give different cooling curves; in particular, different models predict different masses M_{DU} for opening fast neutrino cooling. We have also used a limited set of proton and neutron critical temperature profiles $T_{\mathrm{cn}}(\rho)$ and $T_{\mathrm{cp}}(\rho)$, which are extremely model dependent. This can strongly affect the cooling curves.

5 CONCLUSIONS

We have revised available observational estimates of ages and thermal luminosities of middle-aged cooling INSs and composed a catalogue of their key observational properties for testing theoretical models. A comparison with simulations based on several cooling scenarios shows that the theory can be in good agreement with the data. The estimates of thermal luminosities are usually in better agreement with the cooling theory than temperature estimates for some neutron stars (which may be related to non-uniform temperature distributions over the surfaces of these stars, as discussed in Section 3.1).

The data suggest that the enhanced neutrino emission due to direct Urca reactions operate in some (but not in all) neutron stars, which prompts that these neutron stars are more massive than other, so that the proton fraction in their interiors reaches the values, sufficient to enable the direct Urca processes. The data also favour suppression of the neutron triplet superfluidity, in agreement with recent analyses of smaller observational data sets.

ACKNOWLEDGEMENTS

We thank the referee, Dr. Andreas Reisenegger, for many useful remarks and comments, which helped us to improve the paper. DZ thanks the Pirinem School of Theoretical Physics for hospitality. The work of AP, DZ, and YuS was partially funded by the Russian Foundation for Basic Research and Deutsche Forschungsgemeinschaft according to the research project 19-52-12013. MB is partially supported by the Consejo Nacional de Ciencia y Tecnología with a CB 2014-1 grant #240512. MB also acknowledges support from a postdoctoral fellowship from Dirección General Asuntos del Personal Académico, Universidad Nacional Autónoma de México.

DATA AVAILABILITY

We present the collected data on a dedicated Web page http://www.ioffe.ru/astro/NSG/thermal/cooldat.html; we are planning to update this page on a regular basis as new observational data on cooling neutron stars appear.

REFERENCES

Abdo A. A. et al., 2010, ApJ, 712, 1209
Abdo A. A. et al., 2012, ApJ, 744, 146
Abdo A. A. et al., 2013, ApJS, 208, 17
Acero F., Lemoine-Goumard M., Renaud M., Ballet J., Hewitt J. W., Rousseau R., Tanaka T., 2015, A&A, 580, A74
Akbal O., Alpar M. A., Buchner S., Pines D., 2017, MNRAS, 469, 4183
Allen G. E., Chow K., DeLaney T., Filipović M. D., Houck J. C., Pannuti T. G., Stage M. D., 2015, ApJ, 798, 82
Arnaud K. A., 1996, in Jacoby G. H., Barnes J., eds, ASP Conf. Ser. Vol. 101, Astronomical Data Analysis Software and Systems V. Astron. Soc. Pac., San Fransisco, p. 17
Arumugasamy P., 2015, PhD thesis, The Pennsylvania State University
Arumugasamy P., Kargaltsev O., Posselt B., Pavlov G. G., Hare J., 2018, ApJ, 869, 97
Aschenbach B., 2002, in Becker W., Lesch H., Trümper J., eds, Proceedings of the 270. WE-Heraeus Seminar on Neutron Stars, Pulsars, and Supernova Remnants, MPE, Garching bei Muenchen, p. 13
Aschenbach B., Egger R., Trümper J., 1995, Nature, 373, 587
Ashworth W. B., 1980, J. Hist. Astron., 11, 1
Baldo M., Schulze H.-J., 2007, Phys. Rev. C, 75, 025802
Becker W., Truemper J., 1997, A&A, 326, 682
Becker W., Weisskopf M. C., Tennant A. F., Jessner A., Dyks J., Harding A. K., Zhang S. N., 2004, ApJ, 615, 908
Becker W., Prinz T., Winkler P. F., Petre R., 2012, ApJ, 755, 141
Beronya D. M., Shibanov Y. A., Zyuzin D. A., Komarova V. N., 2015, J. Phys., 661, 012001
Beznogov M. V., Yakovlev D. G., 2015, MNRAS, 447, 1598
Beznogov M. V., Potekhin A. Y., Yakovlev D. G., 2016, MNRAS, 459, 1569
Beznogov M. V., Rrapaj E., Page D., Reddy S., 2018, Phys. Rev. C, 98, 035802
Beznogov M. V., Page D., Ramirez-Ruiz E., 2020, ApJ, 888, 97
Bisnovatyi-Kogan G. S., 2006, Phys.-Usp., 49, 53
Bogdanov S., 2014, ApJ, 790, 94
Bogdanov S. et al., 2019, ApJ, 877, 69
Borkowski K. J., Reynolds S. P., Williams B. J., Petre R., 2018, ApJ, 868, L21

Caraveo P. A., De Luca A., Marelli M., Bignami G. F., Ray P. S., Saz Parkinson P. M., Kanbach G., 2010, ApJ, 725, L6
Cassam-Chenaï G., Decourchelle A., Ballet J., Sauvageot J.-L., Dubner G., Giacani E., 2004, A&A, 427, 199
Caswell J. L., McClure-Griffiths N. M., Cheung M. C. M., 2004, MNRAS, 352, 1405
Chang P., Bildsten L., 2003, ApJ, 585, 464
Chang P., Bildsten L., Arras P., 2010, ApJ, 723, 719
Chang C., Pavlov G. G., Kargaltsev O., Shibanov Y. A., 2012, ApJ, 744, 81
Chatterjee D., Elghozi T., Novak J., Oertel M., 2015, MNRAS, 447, 3785
Chevalier R. A., 1999, ApJ, 511, 798
Cigan P. et al., 2019, ApJ, 886, 51
Cordes J. M., Lazio T. J. W., 2002, preprint (astro-ph/0207156)
Cordes J. M., Lazio T. J. W., 2003, preprint (astro-ph/0301598)
Cropper M., Zane S., Turolla R., Zampieri L., Chieregato M., Drake J., Treves A., 2007, Ap&SS, 308, 161
Cui Y., Pühlhofer G., Santangelo A., 2016, A&A, 591, A68
Danilenko A. A. et al., 2015, One more neutron star with carbon atmosphere. Report at the conference 'High energy astrophysics today and tomorrow – HEA-15', IKI, Moscow
Danilenko A., Karpova A., Ofengeim D., Shibanov Y., Zyuzin D., 2020, MNRAS, 493, 1874
De Blasio F. V., 2000, A&A, 353, 1129
De Luca A., Caraveo P. A., Mereghetti S., Negroni M., Bignami G. F., 2005, ApJ, 623, 1051
De Luca A. et al., 2012, MNRAS, 421, L72
De Luca A. et al., 2013, ApJ, 765, L19
Deller A. T. et al., 2019, ApJ, 875, 100
Ding D., Rios A., Dussan H., Dickhoff W. H., Witte S. J., Carbone A., Polls A., 2016, Phys. Rev. C, 94, 025802
Doroshenko V., Suleimanov V., Santangelo A., 2018, A&A, 618, A76
Durant M., Kargaltsev O., Pavlov G. G., Kowalski P. M., Posselt B., van Kerkwijk M. H., Kaplan D. L., 2012, ApJ, 746, 6
Espinoza C. M., Lyne A. G., Stappers B. W., 2017, MNRAS, 466, 147
Esposito P., De Luca A., Tiengo A., Paizis A., Mereghetti S., Caraveo P. A., 2008, MNRAS, 384, 225
Fesen R. A., 1984, ApJ, 281, 658
Fesen R. A. et al., 2006, ApJ, 645, 283
Fesen R. A., Weil K. E., Cisneros I. A., Blair W. P., Raymond J. C., 2018, MNRAS, 481, 1786
Fortin M., Taranto G., Burgio G. F., Haensel P., Schulze H.-J., Zdunik J. L., 2018, MNRAS, 475, 5010
Foster T., MacWilliams J., 2006, ApJ, 644, 214
Fukui Y. et al., 2012, ApJ, 746, 82
Gaensler B. M., Brazier K. T. S., Manchester R. N., Johnston S., Green A. J., 1999, MNRAS, 305, 724
Gaensler B. M. et al., 2008, ApJ, 680, L37
Gandolfi S., Illarionov A. Y., Pederiva F., Schmidt K. E., Fantoni S., 2009, Phys. Rev. C, 80, 045802
Gençali A. A., Ertan Ü., 2018, MNRAS, 481, 244
Giacani E. B., Dubner G. M., Green A. J., Goss W. M., Gaensler B. M., 2000, AJ, 119, 281
Giacani E., Smith M. J. S., Dubner G., Loiseau N., Castelletti G., Paron S., 2009, A&A, 507, 841
Gnedin O. Y., Yakovlev D. G., Potekhin A. Y., 2001, MNRAS, 324, 725
Gonzalez D., Reisenegger A., 2010, A&A, 522, A16
González-Caniulef D., Guillot S., Reisenegger A., 2019, MNRAS, 490, 5848
González-Jiménez N., Petrovich C., Reisenegger A., 2015, MNRAS, 447, 2073
Graczyk D. et al., 2014, ApJ, 780, 59
Green D. A., Gull S. F., 1982, Nature, 299, 606
Greenstein G., Hartke G. J., 1983, ApJ, 271, 283
Grigorian H., Voskresensky D. N., Maslov K. A., 2018, Nucl. Phys. A, 980, 105
Gudmundsson E. H., Pethick C. J., Epstein R. I., 1983, ApJ, 272, 286
Guillot S., Pavlov G. G., Reyes C., Reisenegger A., Rodriguez L. E., Rangelov B., Kargaltsev O., 2019, ApJ, 874, 175
H. E. S. S. Collaboration, 2011, A&A, 531, A81
Haberl F., 2007, Ap&SS, 308, 181
Haberl F. et al., 2004, A&A, 424, 635
Hachisuka K. et al., 2006, ApJ, 645, 337
Haensel P., 1995, Space Sci. Rev., 74, 427
Haensel P., Potekhin A. Y., Yakovlev D. G., 2007, Astrophysics Space Science Library, Vol. 326, Neutron Stars. 1. Equation of State and Structure. Springer, New York
Halpern J. P., Gotthelf E. V., 2015, ApJ, 812, 61
Halpern J. P., Gotthelf E. V., Camilo F., Helfand D. J., Ransom S. M., 2004, ApJ, 612, 398
Halpern J. P., Bogdanov S., Gotthelf E. V., 2013, ApJ, 778, 120
Hambaryan V., Suleimanov V., Schwope A. D., Neuhäuser R., Werner K., Potekhin A. Y., 2011, A&A, 534, A74
Hambaryan V., Suleimanov V., Haberl F., Schwope A. D., Neuhäuser R., Hohle M., Werner K., 2017, A&A, 601, A108
Hameury J. M., Heyvaerts J., Bonazzola S., 1983, A&A, 121, 259
Hebbar P. R., Heinke C. O., Ho W. C. G., 2020, MNRAS, 491, 1585
Heinke C. O., Ho W. C. G., 2010, ApJ, 719, L167
Hermsen W. et al., 2017, MNRAS, 466, 1688
Hermsen W. et al., 2018, MNRAS, 480, 3655
Ho W. C. G., 2014, in Petit P., Jardine M., Spruit H. C., eds, Proc. IAU Symp., Vol. 302, Magnetic Fields throughout Stellar Evolution. Kluwer, Dordrecht. p. 435
Ho W. C. G., Heinke C. O., 2009, Nature, 462, 71
Ho W. C. G., Kaplan D. L., Chang P., van Adelsberg M., Potekhin A. Y., 2007, MNRAS, 375, 821
Ho W. C. G., Potekhin A. Y., Chabrier G., 2008, ApJS, 178, 102
Ho W. C. G., Elshamouty K. G., Heinke C. O., Potekhin A. Y., 2015, Phys. Rev. C, 91, 015806
Ho W. C. G., Heinke C. O., Chugunov A. I., 2019, ApJ, 882, 128
Hohle M. M., Haberl F., Vink J., de Vries C. P., Neuhäuser R., 2012a, MNRAS, 419, 1525
Hohle M. M., Haberl F., Vink J., de Vries C. P., Turolla R., Zane S., Méndez M., 2012b, MNRAS, 423, 1194
Hui C. Y., Becker W., 2007, A&A, 467, 1209
Hui C. Y., Huang R. H. H., Trepl L., Tetzlaff N., Takata J., Wu E. M. H., Cheng K. S., 2012, ApJ, 747, 74
Hu C.-P., Ng C.-Y., Takata J., Shannon R. M., Johnston S., 2017, ApJ, 838, 156
Igoshev A. P., Tsygankov S. S., Rigoselli M., Mereghetti S., Popov S. B., Elfritz J. G., Mushtukov A. A., 2018, ApJ, 865, 116
Jenkins E. B., Silk J., Wallerstein G., 1976, ApJS, 32, 681
Kaplan D. L., van Kerkwijk M. H., 2009, ApJ, 705, 798
Kaplan D. L., van Kerkwijk M. H., 2011, ApJ, 740, L30
Kaplan D. L., Kamble A., van Kerkwijk M. H., Ho W. C. G., 2011, ApJ, 736, 117
Kargaltsev O., Pavlov G., 2007, Ap&SS, 308, 287
Kargaltsev O., Pavlov G. G., Romani R. W., 2004, ApJ, 602, 327
Kargaltsev O., Durant M., Misanovic Z., Pavlov G. G., 2012, Science, 337, 946
Karpova A., Danilenko A., Shibanov Y., Shternin P., Zyuzin D., 2014, ApJ, 789, 97
Karpova A., Zyuzin D., Danilenko A., Shibanov Y., 2015, MNRAS, 453, 2241
Kaspi V. M., Beloborodov A. M., 2017, ARA&A, 55, 261
Kirichenko A., Danilenko A., Shibanov Y., Shternin P., Zharikov S., Zyuzin D., 2014, A&A, 564, A81
Kirichenko A. et al., 2015, ApJ, 802, 17
Klochkov D., Suleimanov V., Pühlhofer G., Yakovlev D. G., Santangelo A., Werner K., 2015, A&A, 573, A53
Klochkov D., Suleimanov V., Sasaki M., Santangelo A., 2016, A&A, 592, L12
Kochanek C. S., Auchettl K., Belczynski K., 2019, MNRAS, 485, 5394
Kothes R., 2013, A&A, 560, A18
Kramer M., Lyne A. G., Hobbs G., Löhmer O., Carr P., Jordan C., Wolszczan A., 2003, ApJ, 593, L31
Kumar H. S., Safi-Harb S., Gonzalez M. E., 2012, ApJ, 754, 96

Lazendic J. S., Slane P. O., Gaensler B. M., Plucinsky P. P., Hughes J. P., Galloway D. K., Crawford F., 2003, ApJ, 593, L27
Leinson L. B., 2010, Phys. Rev. C, 81, 025501
Leinson L. B., 2016, preprint (arXiv:1611.03794)
Li X., Levin Y., Beloborodov A. M., 2016, ApJ, 833, 189
Li X. H., Lu F. J., Li T. P., 2005, ApJ, 628, 931
Lin L. C. C., Huang R. H. H., Takata J., Hwang C. Y., Kong A. K. H., Hui C. Y., 2010, ApJ, 725, L1
Lin L. C. C. et al., 2012, MNRAS, 426, 2283
Lin Y. C. et al., 1992, IAU Circ., No. 5676, #2
Livingstone M. A., Kaspi V. M., 2011, ApJ, 742, 31
Lovchinsky I., Slane P., Gaensler B. M., Hughes J. P., Ng C.-Y., Lazendic J. S., Gelfand J. D., Brogan C. L., 2011, ApJ, 731, 70
Malacaria C. et al., 2019, ApJ, 880, 74
Manchester R. N., Taylor J. H. J., 1977, Pulsars. W. H. Freeman & Co., San Francisco
Manchester R. N., Hobbs G. B., Teoh A., Hobbs M., 2005, AJ, 129, 1993
Manzali A., De Luca A., Caraveo P. A., 2007, ApJ, 669, 570
Marelli M., Mignani R. P., De Luca A., Saz Parkinson P. M., Salvetti D., Den Hartog P. R., Wolff M. T., 2015, ApJ, 802, 78
Margueron J., Sagawa H., Hagino K., 2008, Phys. Rev. C, 77, 054309
Martín J., Torres D. F., Pedaletti G., 2016, MNRAS, 459, 3868
Maxted N. I. et al., 2013, Publ. Astron. Soc. Aust., 30, e055
Maxted N. et al., 2018, MNRAS, 474, 662
McClure-Griffiths N. M., Green A. J., Dickey J. M., Gaensler B. M., Haynes R. F., Wieringa M. H., 2001, ApJ, 551, 394
McGowan K. E., Zane S., Cropper M., Kennea J. A., Córdova F. A., Ho C., Sasseen T., Vestrand W. T., 2004, ApJ, 600, 343
McGowan K. E., Zane S., Cropper M., Vestrand W. T., Ho C., 2006, ApJ, 639, 377
Meisel Z., Deibel A., Keek L., Shternin P., Elfritz J., 2018, J. Phys. G, 45, 093001
Mereghetti S., De Luca A., Caraveo P. A., Becker W., Mignani R., Bignami G. F., 2002, ApJ, 581, 1280
Mereghetti S., Pons J. A., Melatos A., 2015, Space Sci. Rev., 191, 315
Migliazzo J. M., Gaensler B. M., Backer D. C., Stappers B. W., van der Swaluw E., Strom R. G., 2002, ApJ, 567, L141
Mignani R. P., Pavlov G. G., Kargaltsev O., 2010, ApJ, 720, 1635
Mignani R. P. et al., 2013, MNRAS, 429, 3517
Miller J. J., McLaughlin M. A., Rea N., Lazaridis K., Keane E. F., Kramer M., Lyne A., 2013, ApJ, 776, 104
Mirabal N., Halpern J. P., 2000, BAAS. 1509
Misanovic Z., Pavlov G. G., Garmire G. P., 2008, ApJ, 685, 1129
Misner C. W., Thorne K. S., Wheeler J. A., 1973, Gravitation. W. H. Freeman and Co., San Francisco
Mori K. et al., 2014, ApJ, 793, 88
Moriguchi Y., Tamura K., Tawara Y., Sasago H., Yamaoka K., Onishi T., Fukui Y., 2005, ApJ, 631, 947
Motch C., Sekiguchi K., Haberl F., Zavlin V. E., Schwope A., Pakull M. W., 2005, A&A, 429, 257
Motch C., Pires A. M., Haberl F., Schwope A., Zavlin V. E., 2009, A&A, 497, 423
Ng C.-Y., Romani R. W., Brisken W. F., Chatterjee S., Kramer M., 2007, ApJ, 654, 487
Ng C.-Y., Kaspi V. M., Ho W. C. G., Weltevrede P., Bogdanov S., Shannon R., Gonzalez M. E., 2012, ApJ, 761, 65
Ofengeim D. D., Zyuzin D. A., 2018, Particles, 1, 194
Page D., 2009, in Becker W., ed., Astrophysics Space Science Library, Vol. 357, Neutron Stars and Pulsars, Springer, Berlin, p. 247
Page D., 2016, Astrophysics Source Code Library, record ascl:1609.009
Page D., Lattimer J. M., Prakash M., Steiner A. W., 2004, ApJS, 155, 623
Page D., Prakash M., Lattimer J. M., Steiner A. W., 2011, Phys. Rev. Lett., 106, 081101
Page D., Lattimer J. M., Prakash M., Steiner A. W., 2014, in Bennemann K.-H., Ketterson J. B., eds, International Series of Monographs on Physics, Vol. 2, Novel Superfluids, Oxford University Press, Oxford, p. 505
Page D., Beznogov M. V., Garibay I., Lattimer J. M., Prakash M., Janka H.-T., 2020, ApJ, preprint (arXiv:2004.06078)
Pavlov G. G., Kargaltsev O., Brisken W. F., 2008, ApJ, 675, 683
Pavlov G. G., Rangelov B., Kargaltsev O., Reisenegger A., Guillot S., Reyes C., 2017, ApJ, 850, 79
Pearson J. M., Chamel N., Potekhin A. Y., Fantina A. F., Ducoin C., Dutta A. K., Goriely S., 2018, MNRAS, 481, 2994
Pineault S., Landecker T. L., Madore B., Gaumont-Guay S., 1993, AJ, 105, 1060
Pires A. M., Motch C., Turolla R., Popov S. B., Schwope A. D., Treves A., 2015, A&A, 583, A117
Pires A. M., Schwope A. D., Haberl F., Zavlin V. E., Motch C., Zane S., 2019, A&A, 623, A73
Pons J. A., Viganò D., 2019, Living Rev. Comput. Astrophys., 5, 3
Posselt B., Pavlov G. G., 2018, ApJ, 864, 135
Posselt B., Popov S. B., Haberl F., Trümper J., Turolla R., Neuhäuser R., 2007, Ap&SS, 308, 171
Posselt B., Pavlov G. G., Suleimanov V., Kargaltsev O., 2013, ApJ, 779, 186
Potekhin A. Y., 2014, Phys. Usp., 57, 735
Potekhin A. Y., Chabrier G., 2012, A&A, 538, A115
Potekhin A. Y., Chabrier G., 2018, A&A, 609, A74
Potekhin A. Y., Yakovlev D. G., 2001, A&A, 374, 213
Potekhin A. Y., Chabrier G., Yakovlev D. G., 1997, A&A, 323, 415
Potekhin A. Y., Yakovlev D. G., Chabrier G., Gnedin O. Y., 2003, ApJ, 594, 404
Potekhin A. Y., Urpin V., Chabrier G., 2005, A&A, 443, 1025
Potekhin A. Y., Pons J. A., Page D., 2015, Space Sci. Rev., 191, 239
Potekhin A. Y., Chugunov A. I., Chabrier G., 2019, A&A, 629, A88
Raduta A. R., Li J. J., Sedrakian A., Weber F., 2019, MNRAS, 487, 2639
Rangelov B., Pavlov G. G., Kargaltsev O., Reisenegger A., Guillot S., van Kerkwijk M. H., Reyes C., 2017, ApJ, 835, 264
Reed J. E., Hester J. J., Fabian A. C., Winkler P. F., 1995, ApJ, 440, 706
Reich W., Braunsfurth E., 1981, A&A, 99, 17
Reimer O., Brazier K. T. S., Carramiñana A., Kanbach G., Nolan P. L., Thompson D. J., 2001, MNRAS, 324, 772
Reynoso E. M., Green A. J., Johnston S., Dubner G. M., Giacani E. B., Goss W. M., 2003, MNRAS, 345, 671
Richardson M. B., van Horn H. M., Ratcliff K. F., Malone R. C., 1982, ApJ, 255, 624
Rigoselli M., Mereghetti S., 2018, A&A, 615, A73
Rigoselli M., Mereghetti S., Suleimanov V., Potekhin A. Y., Turolla R., Taverna R., Pintore F., 2019a, A&A, 627, A69
Rigoselli M., Mereghetti S., Turolla R., Taverna R., Suleimanov V., Potekhin A. Y., 2019b, ApJ, 872, 15
Roberts D. A., Goss W. M., Kalberla P. M. W., Herbstmeier U., Schwarz U. J., 1993, A&A, 274, 427
Roger R. S., Milne D. K., Kesteven M. J., Wellington K. J., Haynes R. F., 1988, ApJ, 332, 940
Rutledge R. E., Fox D. B., Shevchuk A. H., 2008, ApJ, 672, 1137
Salmi T., Suleimanov V. F., Nättilä J., Poutanen J., 2020, A&A, preprint (arXiv:2002.11427)
Sartore N., Tiengo A., Mereghetti S., De Luca A., Turolla R., Haberl F., 2012, A&A, 541, A66
Sasaki M., Mäkelä M. M., Klochkov D., Santangelo A., Suleimanov V., 2018, MNRAS, 479, 3033
Schwope A. D. et al., 2009, A&A, 499, 267
Sedrakian A., 2019, Phys. Rev. D, 99, 043011
Sedrakian A., Clark J. W., 2019, Eur. Phys. J. A, 55, 167
Shibanov Y. A., Sollerman J., Lundqvist P., Gull T., Lindler D., 2005, A&A, 440, 693
Shibanov Y., Danilenko A., Zharikov S., Shternin P., Zyuzin D., 2016, ApJ, 831, 112
Shternin P. S., Yakovlev D. G., Heinke C. O., Ho W. C. G., Patnaude D. J., 2011, MNRAS, 412, L108
Shternin P. S., Baldo M., Haensel P., 2018, Phys. Lett. B, 786, 28
Shternin P., Kirichenko A., Zyuzin D., Yu M., Danilenko A., Voronkov M., Shibanov Y., 2019, ApJ, 877, 78
Slane P., Gaensler B. M., Dame T. M., Hughes J. P., Plucinsky P. P., Green A., 1999, ApJ, 525, 357

Slane P., Helfand D. J., van der Swaluw E., Murray S. S., 2004, ApJ, 616, 403
Smith N., 2006, ApJ, 644, 1151
Speagle J. S., Kaplan D. L., van Kerkwijk M. H., 2011, ApJ, 743, 183
Stephenson F. R., 1971, QJRAS, 12, 10
Stephenson F. R., Green D. A., 2003, J. Astron. Hist. Heritage, 6, 46
Stothers R., 1980, PASP, 92, 145
Strom R. G., Stappers B. W., 2000, in Kramer M., Wex N., Wielebinski R., eds, ASP Conf. Ser. Vol. 202, IAU Colloq. 177: Pulsar Astronomy – 2000 and Beyond. Astron. Soc. Pac., San Fransisco, p. 509
Suleimanov V. F., Klochkov D., Pavlov G. G., Werner K., 2014, ApJS, 210, 13
Sun M., Seward F. D., Smith R. K., Slane P. O., 2004, ApJ, 605, 742
Swartz D. A. et al., 2015, ApJ, 808, 84
Szary A., Gil J., Zhang B., Haberl F., Melikidze G. I., Geppert U., Mitra D., Xu R.-X., 2017, ApJ, 835, 178
Takatsuka T., Tamagaki R., 2004, Prog. Theor. Phys., 112, 37
Tanaka S. J., Takahara F., 2013, MNRAS, 429, 2945
Taranto G., Burgio G. F., Schulze H.-J., 2016, MNRAS, 456, 1451
Testa V., Mignani R. P., Rea N., Marelli M., Salvetti D., Breeveld A. A., Cusano F., Carini R., 2018, MNRAS, 473, 2000
Tetzlaff N., Eisenbeiss T., Neuhäuser R., Hohle M. M., 2011, MNRAS, 417, 617
Tetzlaff N., Schmidt J. G., Hohle M. M., Neuhäuser R., 2012, Publ. Astron. Soc. Aust., 29, 98
Thorne K. S., 1977, ApJ, 212, 825
Tian W. W., Leahy D. A., Haverkorn M., Jiang B., 2008, ApJ, 679, L85
Timokhin A. N., Arons J., 2013, MNRAS, 429, 20
Trimble V., 1973, PASP, 85, 579
Tsuruta S., 2009, in Becker W., ed., Astrophysics Space Sci. Library, Vol. 357, Neutron Stars and Pulsars, Springer, Berlin, p. 289
Turolla R., 2009, in Becker W., ed., Astrophysics Space Sci. Library, Vol. 357, Neutron Stars and Pulsars, Springer, Berlin, p. 141
Van Etten A., Romani R. W., Ng C.-Y., 2008, ApJ, 680, 1417
van Kerkwijk M. H., Kaplan D. L., 2008, ApJ, 673, L163
Verbiest J. P. W., Weisberg J. M., Chael A. A., Lee K. J., Lorimer D. R., 2012, ApJ, 755, 39
Viganò D., Rea N., Pons J. A., Perna R., Aguilera D. N., Miralles J. A., 2013, MNRAS, 434, 123
Vogt F. P. A., Bartlett E. S., Seitenzahl I. R., Dopita M. A., Ghavamian P., Ruiter A. J., Terry J. P., 2018, Nat. Astron., 2, 465
Walter F. M., Wolk S. J., Neuhäuser R., 1996, Nature, 379, 233
Walter F. M., Eisenbeiß T., Lattimer J. M., Kim B., Hambaryan V., Neuhäuser R., 2010, ApJ, 724, 669
Wang Z. R., Qu Q. Y., Chen Y., 1997, A&A, 318, L59
Webb N. A., Leahy D., Guillot S., Baillot d'Etivaux N., Barret D., Guillemot L., Margueron J., Miller M. C., 2019, A&A, 627, A141
Wei J. B., Burgio G. F., Schulze H. J., 2019, MNRAS, 484, 5162
Wei J. B., Burgio G. F., Schulze H. J., Zappalà D., 2020, MNRAS, preprint (arXiv:2003.08079)
Weisskopf M. C., Tennant A. F., Yakovlev D. G., Harding A., Zavlin V. E., O'Dell S. L., Elsner R. F., Becker W., 2011, ApJ, 743, 139
Welsh B. Y., Sallmen S., 2003, A&A, 408, 545
Wijngaarden M. J. P., Ho W. C. G., Chang P., Heinke C. O., Page D., Beznogov M., Patnaude D. J., 2019, MNRAS, 484, 974
Williams B. J., Hewitt J. W., Petre R., Temim T., 2018, ApJ, 855, 118
Wilms J., Allen A., McCray R., 2000, ApJ, 542, 914
Xi L., Gaetz T. J., Plucinsky P. P., Hughes J. P., Patnaude D. J., 2019, ApJ, 874, 14
Xu Y., Reid M. J., Zheng X. W., Menten K. M., 2006, Science, 311, 54
Yakovlev D. G., Pethick C. J., 2004, ARA&A, 42, 169
Yakovlev D. G., Kaminker A. D., Gnedin O. Y., Haensel P., 2001, Phys. Rep., 354, 1
Yakovlev D. G., Levenfish K. P., Haensel P., 2003, A&A, 407, 265
Yanagi K., Nagata N., Hamaguchi K., 2020, MNRAS, 492, 5508
Yao J. M., Manchester R. N., Wang N., 2017, ApJ, 835, 29
Yar-Uyaniker A., Uyaniker B., Kothes R., 2004, ApJ, 616, 247
Yoneyama T., Hayashida K., Nakajima H., Inoue S., Tsunemi H., 2017, PASJ, 69, 50
Zampieri L., Campana S., Turolla R., Chieregato M., Falomo R., Fugazza D., Moretti A., Treves A., 2001, A&A, 378, L5
Zane S. et al., 2011, MNRAS, 410, 2428
Zavlin V. E., 2007, ApJ, 665, L143
Zavlin V. E., 2009, in Becker W., ed., Astrophysics Space Sci. Library, Vol. 357, Neutron Stars and Pulsars, Springer, Berlin, p. 181
Zavlin V. E., Pavlov G. G., 2004, Mem. Soc. Astron. Ital., 75, 458
Zavlin V. E., Pavlov G. G., Shibanov Y. A., 1996, A&A, 315, 141
Zhu W. W., Kaspi V. M., McLaughlin M. A., Pavlov G. G., Ng C. Y., Manchester R. N., Gaensler B. M., Woods P. M., 2011, ApJ, 734, 44
Zyuzin D. A., Karpova A. V., Shibanov Y. A., 2018, MNRAS, 476, 2177
Zyuzin D. A., Karpova A. V., Shibanov Y. A., Potekhin A. Y., 2019, Very cold gamma pulsar PSR J1957+5033, Report at the conference 'High energy astrophysics today and tomorrow – HEA-19', IKI, Moscow

This paper has been typeset from a TEX/LATEX file prepared by the author.